

# *Bacillus anthracis* Inosine 5'-Monophosphate Dehydrogenase in Action: The First Bacterial Series of Structures of Phosphate Ion-, Substrate-, and Product-Bound Complexes

Magdalena Makowska-Grzyska,<sup>†</sup> Youngchang Kim,<sup>†,‡</sup> Ruiying Wu,<sup>‡</sup> Rosemarie Wilton,<sup>‡</sup> Deviprasad R. Gollapalli,<sup>§</sup> Ximi K. Wang,<sup>§</sup> Rongguang Zhang,<sup>‡</sup> Robert Jedrzejczak,<sup>‡</sup> Jamey C. Mack,<sup>‡,+</sup> Natalia Maltseva,<sup>†</sup> Rory Mulligan,<sup>†</sup> T. Andrew Binkowski,<sup>†,‡</sup> Piotr Gornicki,<sup>||</sup> Misty L. Kuhn,<sup>⊥</sup> Wayne F. Anderson,<sup>⊥</sup> Lizbeth Hedstrom,<sup>§,@</sup> and Andrzej Joachimiak<sup>\*,†,‡</sup>

<sup>†</sup>Center for Structural Genomics of Infectious Diseases, University of Chicago, 5735 South Ellis Avenue, Chicago, Illinois 60637, United States

<sup>‡</sup>Midwest Center for Structural Genomics, Argonne National Laboratory, 9700 South Cass Avenue, Building 202, Argonne, Illinois 60439, United States

<sup>§</sup>Department of Biology, Brandeis University, 415 South Street, Waltham, Massachusetts 02454-9110, United States

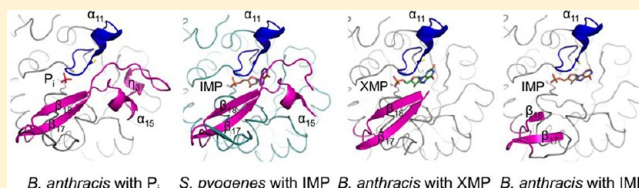
<sup>||</sup>Department of Molecular Genetics and Cell Biology, University of Chicago, 920 East 58th Street, Chicago, Illinois 60637, United States

<sup>⊥</sup>Department of Molecular Pharmacology and Biological Chemistry, Northwestern University Feinberg School of Medicine, Chicago, Illinois 60611, United States

<sup>@</sup>Department of Chemistry, Center for Structural Genomics of Infectious Diseases, Brandeis University, 415 South Street, Waltham, Massachusetts 02454-9110, United States

## Supporting Information

**ABSTRACT:** Inosine 5'-monophosphate dehydrogenase (IMPDH) catalyzes the first unique step of the GMP branch of the purine nucleotide biosynthetic pathway. This enzyme is found in organisms of all three kingdoms. IMPDH inhibitors have broad clinical applications in cancer treatment, as antiviral drugs and as immunosuppressants, and have also displayed antibiotic activity. We have determined three crystal structures of *Bacillus anthracis* IMPDH, in a phosphate ion-bound (termed "apo") form and in complex with its substrate, inosine 5'-monophosphate (IMP), and product, xanthosine 5'-monophosphate (XMP). This is the first example of a bacterial IMPDH in more than one state from the same organism. Furthermore, for the first time for a prokaryotic enzyme, the entire active site flap, containing the conserved Arg-Tyr dyad, is clearly visible in the structure of the apoenzyme. Kinetic parameters for the enzymatic reaction were also determined, and the inhibitory effect of XMP and mycophenolic acid (MPA) has been studied. In addition, the inhibitory potential of two known *Cryptosporidium parvum* IMPDH inhibitors was examined for the *B. anthracis* enzyme and compared with those of three bacterial IMPDHs from *Campylobacter jejuni*, *Clostridium perfringens*, and *Vibrio cholerae*. The structures contribute to the characterization of the active site and design of inhibitors that specifically target *B. anthracis* and other microbial IMPDH enzymes.



*B. anthracis* with  $P_i$  *S. pyogenes* with IMP *B. anthracis* with XMP *B. anthracis* with IMP

Inosine 5'-monophosphate dehydrogenase (IMPDH, EC 1.1.1.205) catalyzes the oxidation of inosine 5'-monophosphate (IMP) to xanthosine 5'-monophosphate (XMP) with the concomitant reduction of  $NAD^+$  to NADH. The reaction is a branch point between the adenine and guanine nucleotide biosynthesis, and a rate-limiting step of GMP biosynthesis. As a regulator of the intracellular guanine nucleotide pool, IMPDH is crucial for DNA and RNA synthesis, signal transduction, and other processes involved in cell proliferation. Inhibition of IMPDH causes an overall reduction in the size of guanine nucleotide pools, and as GTP is a cofactor in the conversion of IMP to AMP, adenylate pools are also affected.<sup>1,2</sup> Many inhibitors of human IMPDHs are

used clinically as anticancer and immunosuppressive agents.<sup>1,3–6</sup> IMPDH is also a potential antibacterial target.<sup>7</sup>

Discovery of new antibiotic drugs against *Bacillus anthracis*, the causative agent of anthrax, is an important goal of the biodefense program.<sup>8,9</sup> Mycophenolic acid (MPA), a potent inhibitor of eukaryotic IMPDHs, has antibacterial activity against *B. anthracis*<sup>10</sup> and *Staphylococcus aureus*.<sup>11,12</sup> However,

**Received:** April 19, 2012

**Revised:** June 8, 2012

**Published:** July 12, 2012

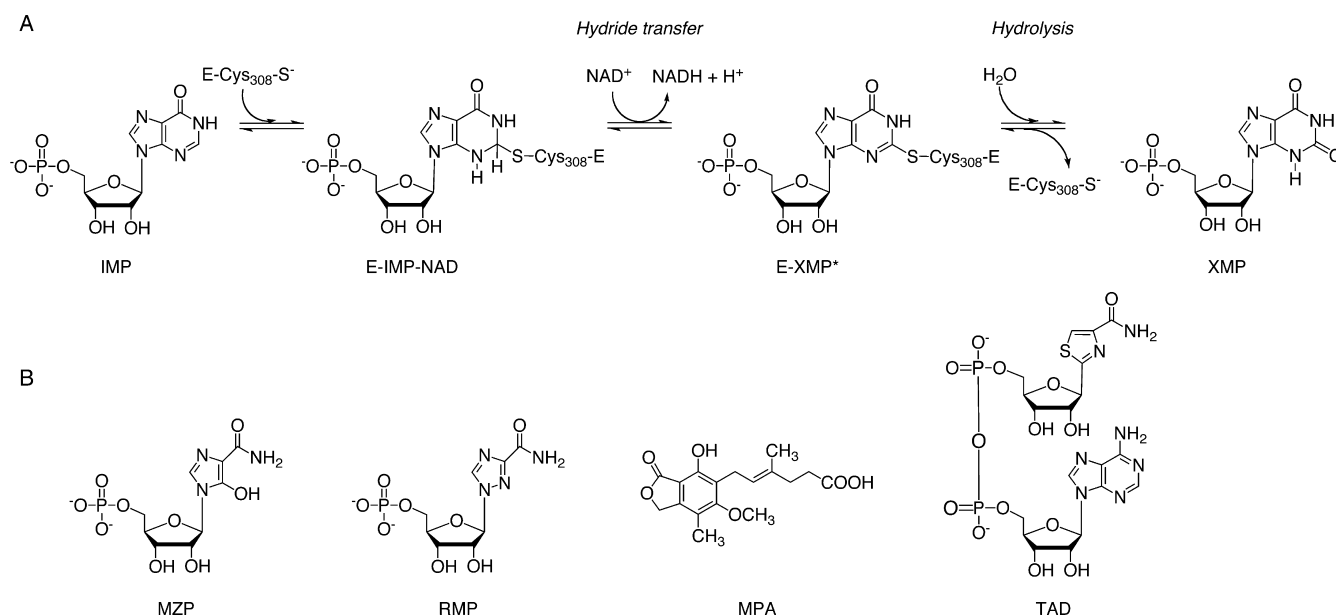


**Figure 1.** (A) Mechanism of the IMPDH reaction. The covalent enzyme–thioimidate intermediate is shown as E-XMP\*. (B) *anthracis* numbering is used. (B) Inhibitors targeting human IMPDH.

new antibiotics are needed to combat the emergence of multidrug resistant bacteria.

Crystal structures of IMPDH enzymes from several organisms in complex with substrates, cofactors, and inhibitors have been determined.<sup>13–22</sup> IMPDH is a homotetramer with 4-fold symmetry. Most IMPDH monomers contain two domains: the catalytic domain, which is a classic eight-fold  $\beta/\alpha$ -barrel (TIM barrel),<sup>23</sup> and the CBS subdomain (homologous to a domain in cystathionine  $\beta$ -synthase).<sup>24,25</sup> The active site is composed of residues located in loops on the proximal face of the TIM barrel near the C-terminal end with the adjacent subunits also contributing residues. The active site loops are disordered in most IMPDH structures, indicating conformational flexibility required by the IMPDH-catalyzed reaction. Binding of the substrate and the cofactor results in conformational changes involving two mobile elements of the IMPDH active site, with one being the active site loop containing catalytic Cys308 (residues 302–317 in *B. anthracis* numbering) and the second, another loop, commonly called the active site “flap” (residues 380–430). Interactions mediated by these loops in the substrate–cofactor complexes vary between IMPDH enzymes from different sources (bacterial vs human), and they are partly responsible for a different sensitivity of these enzymes to inhibitors.<sup>26</sup>

The mechanism of IMPDH has been studied extensively (reviewed in ref 3). It involves a two-step reaction that consists of a fast redox step and a rate-limiting hydrolysis step. Cys308 from the active site loop attacks C2 of IMP and forms a covalent adduct. The NAD<sup>+</sup> cofactor is bound; a hydride ion is transferred from C2 to NAD<sup>+</sup>, and NADH is released (Figure 1). The catalytic flap moves into the site previously occupied by NADH, positioning a conserved Arg-Tyr dyad (*B. anthracis* residues 404 and 405, respectively) in the active site for hydrolysis of the covalently bound thioimidate intermediate, E-XMP\* (Figure 1).<sup>3,27</sup> An active site water molecule activated through proton abstraction by the catalytic dyad hydrolyzes E-XMP\*,<sup>20,28,29</sup> and XMP is released. IMPDH catalyzes two very different chemical transformations, and the enzyme has two mutually exclusive conformations, an open conformation for

ligand binding, redox reaction, and product release and a closed conformation for hydrolysis.<sup>3</sup> Both of these conformations can be targeted for inhibitors.

All IMPDH enzymes require monovalent cations such as K<sup>+</sup> for activity. The ion is proposed to play a dynamic role, possibly binding transiently near the active site cysteine residue, stabilizing the E-XMP\* complex, and influencing NAD<sup>+</sup> binding.<sup>30,31</sup>

Although IMPDHs from all organisms are similar in sequence and structure, the eukaryotic and prokaryotic enzymes differ significantly in their kinetic properties and sensitivity to inhibitors.<sup>3,7,32</sup> For example, mycophenolic acid (MPA) is a significantly more potent inhibitor of the human enzyme than the bacterial IMPDHs.<sup>7,15</sup> MPA binds in the nicotinamide portion of the NAD<sup>+</sup> binding pocket and traps the E-XMP\* intermediate.<sup>33,34</sup> The selectivity of MPA stems from its competition with the flap for the NAD<sup>+</sup> site. Because the closed conformation is required for the hydrolysis of E-XMP\*, hydrolysis will occur faster in the enzymes in which the closed conformation is preferred. Human IMPDHs favor the open conformation, while bacterial enzymes prefer the closed one.<sup>7,35</sup> The closed conformation makes the prokaryotic IMPDHs resistant to MPA.<sup>3</sup>

Thus far, parasite-specific inhibitors have only been reported for *Cryptosporidium parvum*. The X-ray structure of *C. parvum* IMPDH in complex with IMP and one such inhibitor, compound C64, revealed a new binding mode in which the inhibitor interacts with the purine ring of IMP as expected but bends across Ala165 toward the dimer interface to interact with Tyr358 in the adjacent subunit.<sup>22</sup> Mammalian IMPDHs contain substitutions at positions 165 and 358 (Ala253 and Tyr445, respectively, in *B. anthracis* numbering), which explain their resistance to these inhibitors. *C. parvum* IMPDH is closely related to prokaryotic IMPDHs,<sup>36,37</sup> and the *C. parvum*-specific inhibitors were shown to also inhibit bacterial proteins, such as *Helicobacter pylori*, *Borrelia burgdorferi*, and *Streptococcus pyogenes*.<sup>38</sup> Thus, Ala165 and Tyr358 comprise a structural motif that defines the susceptibility of the enzyme to *C. parvum* inhibitors. Ala165 and Tyr358 are present at corresponding



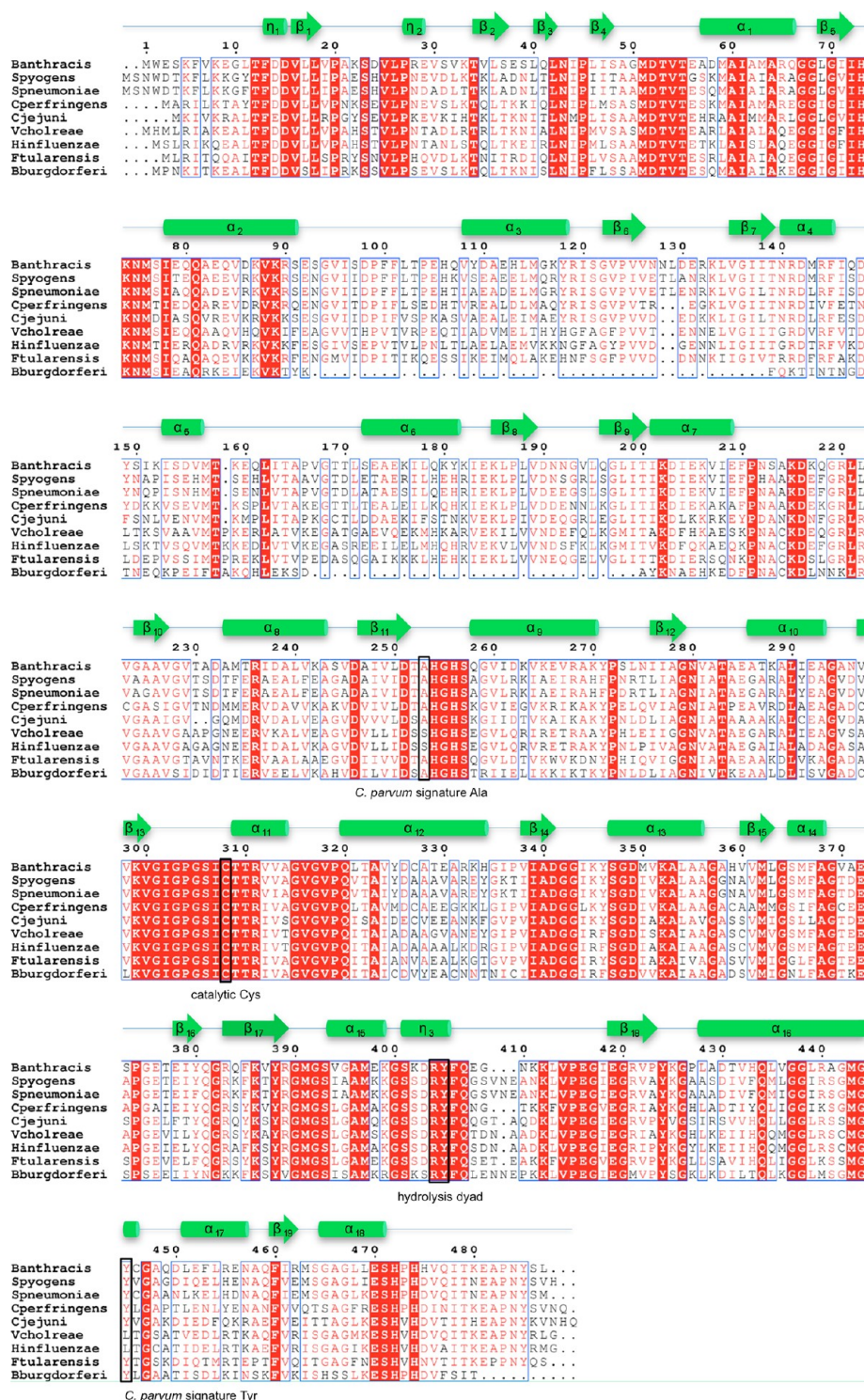


**Figure 2.** Multiple-sequence alignment of IMPDHs from selected bacterial pathogens. The following IMPDH sequences were used in the alignment: *B. anthracis* strain Ames, *S. pyogenes*, *Streptococcus pneumoniae*, *Cl. perfringens*, *Ca. jejuni*, *Vibrio cholerae*, *Haemophilus influenzae*, *Francisella tularensis*, and *Bo. burgdorferi*. Identical residues are highlighted in red, and similar residues are shown as red letters. Secondary structure elements derived from *B. anthracis* IMPDH are depicted as arrows (representing  $\beta$ -strands) and cylinders (representing  $\alpha$ -helices and  $3_{10}$ -helices) and are numbered consecutively. The positions for the active site cysteine, hydrolysis dyad, and residues from the *C. parvum* signature motif are marked as black rectangles and labeled.

positions in IMPDHs from a wide variety of pathogenic bacteria, including *B. anthracis*, *Campylobacter jejuni*, and *Clostridium perfringens* (Figure 2).

Currently, there are no examples of an IMPDH structure in more than one state from the same bacterial species.

Additionally, there has been no comparison of the active site in noncovalently bound substrate and product complexes for a bacterial IMPDH. Here, we report three crystal structures of IMPDH from *B. anthracis*, a phosphate ion-bound ( $P_i$ -bound) form (2.60 Å), which will be interchangeably termed the “apo”

state, and in complex with its substrate (IMP) and product (XMP) (2.38 and 2.65 Å, respectively). We characterize kinetic parameters of the *B. anthracis* enzyme with respect to the substrates IMP and NAD<sup>+</sup>, MPA, and two inhibitors of *C. parvum* IMPDH,<sup>22,39,40</sup> a quinolinium-substituted triazole derivative, A110,<sup>41</sup> and a 2-pyridinyl derivative of benzimidazole, C91<sup>38</sup> (Figure 7). We compare the inhibition properties of *B. anthracis* IMPDH to those of three bacterial enzymes from *Ca. jejuni*, *Cl. perfringens*, and *Vibrio cholerae*, and we show that these enzymes bind inhibitors with very different affinities, indicating that small changes in the active site can influence inhibitor binding.

## MATERIALS AND METHODS

**Materials.** IMP was purchased from Acros Organics. XMP was purchased from Fluka. NAD<sup>+</sup>, NADH, and MPA were purchased from Sigma. Two *C. parvum*-selective inhibitors, compounds A110 (4-((1R)-[1-(4-chlorophenyl)-1H-1,2,3-triazol-4-yl]ethoxy)quinoline-1-oxide, C<sub>19</sub>H<sub>15</sub>ClN<sub>4</sub>O<sub>2</sub>, CAS Registry Number 1185388-35-5) and C91 [ $\alpha$ -methyl-N-2-naphthalenyl-2-(2-pyridinyl)-1H-benzimidazole-1-acetamide, C<sub>24</sub>H<sub>18</sub>N<sub>4</sub>O, CAS Registry Number 125749-66-9], were synthesized as described in refs 41 and 38, respectively. Crystallization reagents were purchased from Hampton Research (Aliso Viejo, CA) and Microlytic (Woburn, MA).

**Gene Cloning, Protein Expression, Purification, and Crystallization.** The coding sequences of IMPDH enzymes were amplified by polymerase chain reaction (PCR) from chromosomal DNA of *B. anthracis* (strain Sterne), *Ca. jejuni*, *Cl. perfringens*, and *V. cholerae* using primers compatible with the ligation-independent cloning vector pMCSG7.<sup>42</sup> The genes were cloned into pMCSG7 using a modified ligation-independent cloning protocol.<sup>42</sup> The recombinant constructs produced fusion proteins with an N-terminal His<sub>6</sub> tag and a TEV protease recognition site (ENLYFQJ<sub>S</sub>). The fusion proteins were expressed in *Escherichia coli* strain BL21(DE3) harboring the pMAGIC plasmid encoding one rare *E. coli* Arg tRNA (covering codons AGG/AGA) in the presence of 100  $\mu$ g/mL ampicillin and 30  $\mu$ g/mL kanamycin. The cells were grown in LB medium at 37 °C to an OD<sub>600</sub> of 0.6–0.8. This was followed by overnight induction with 0.5 mM isopropyl  $\beta$ -D-thiogalactoside (IPTG) at 20 °C. Cells were harvested, resuspended in lysis buffer [50 mM Hepes (pH 8.0), 500 mM NaCl, 10 mM imidazole, 10 mM 2-mercaptoethanol, and 5% glycerol], and stored at –80 °C.

The selenomethionine (SeMet) derivative of *B. anthracis* IMPDH was prepared as described previously.<sup>43</sup> The BL21-(DE3)/pMAGIC cells were grown at 37 °C in M9 medium supplemented with 0.4% glucose, 8.5 mM NaCl, 0.1 mM CaCl<sub>2</sub>, 2 mM MgSO<sub>4</sub>, and 1% thiamine. After the OD<sub>600</sub> reached 0.8, Leu, Ile, Lys, Phe, Thr, and Val each at 0.01% (w/v) were added to inhibit the methionine metabolic pathway and increase the level of SeMet incorporation. SeMet was added to the culture (60 mg of SeMet/L of culture), and 15 min later, protein expression was induced with 0.5 mM IPTG. The culture was then incubated at 18 °C overnight. Cells were harvested, resuspended in lysis buffer, and stored at –80 °C.

For inhibitor binding studies using ForteBio Octet, all IMPDH proteins presented here were expressed from the vector pMCSG50. This vector was constructed by modification of the dual-LIC vector pMCSG60. Vector pMCSG60 contains the SmaI LIC site from pMCSG26<sup>44</sup> downstream from the Ssp I LIC site in pMCSG7,<sup>42</sup> allowing for expression of two

proteins from a single vector. A pair of synthetic oligos encoding a 15-amino acid biotinylation signal<sup>45</sup> and including the His<sub>6</sub> tag was ligated into pMCSG60 between the NdeI and Acc6SI restriction sites of pMCSG60. This regenerated the pMCSG7 LIC site with the biotinylation signal inserted between the His<sub>6</sub> tag and the TEV protease recognition site. The biotin-protein ligase gene (*birA*) was synthesized from *E. coli* BL21 by PCR. The two-step PCR introduced a silent single-base mutation that eliminated the SspI site from the native gene. The *birA* PCR product was cloned into the SmaI LIC site of the new vector using the standard LIC protocol. The resulting plasmid (pMCSG50) retains the standard pMCSG7 LIC site for protein expression and coexpresses the biotin-protein ligase gene. Target protein overexpressed from this plasmid contains a biotinylated tag (GLNDIFEAQ-KIEWR) that is modified at the lysine residue (underlined). The enzymatic activities of the native enzyme and the biotin-labeled derivative were comparable within 10%.

All IMPDH proteins were purified according to a standard protocol.<sup>46</sup> Lysozyme (final concentration of 1 mg/mL) and protease inhibitor cocktail (Roche, Indianapolis, IN; 50 mL/g of wet cells) were added to the thawed cell suspension. The solution was incubated on ice for 20 min and lysed by sonication. The lysate was clarified by centrifugation at 36000g for 1 h and filtered through a 0.44  $\mu$ m membrane. Clarified lysate was applied to a 5 mL HiTrap Ni-NTA column (GE Healthcare Life Sciences, Piscataway, NJ) on an ÄKTAexpress system (GE Healthcare Life Sciences). The column was washed with lysis buffer containing 20 mM imidazole, and the protein was eluted with the same buffer containing 250 mM imidazole. IMPDHs were dialyzed against crystallization buffer containing 20 mM Hepes (pH 8.0), 150 mM KCl, and 2 mM DTT, concentrated, flash-frozen, and stored in liquid nitrogen. The His<sub>6</sub> tag was not cleaved from the protein for either the crystallography or enzyme assays.

Native (i.e., not labeled with SeMet) IMPDH enzyme preparations were used for all enzyme assays, and these were subjected to an additional purification step on a Superdex 300 16/60 size exclusion chromatography column equilibrated with buffer containing 50 mM Tris-HCl (pH 8.0), 100 mM KCl, 1 mM DTT, 3 mM EDTA, and 10% glycerol or containing 20 mM Hepes (pH 8.0), 150 mM KCl, and 2 mM DTT. Fractions containing IMPDH were identified by sodium dodecyl sulfate–polyacrylamide gel electrophoresis, concentrated, and flash-cooled.

Crystallization screens were initially performed by the sitting-drop, vapor-diffusion method at 16 and 18 °C. Crystals containing IMP were optimized using the hanging-drop, vapor-diffusion method. Hanging drops consisted of IMPDH at a concentration of 15 mg/mL and 4 mM IMP mixed with an equal volume of reservoir solution [20% PEG 3350, 0.2 M MgSO<sub>4</sub>, and 0.1 M Tris-HCl (pH 7.6)]. Crystals with XMP were obtained at 16 °C from a sitting-drop solution containing 8 mg/mL protein and 1.6 mM XMP mixed with an equal volume of reservoir solution [0.5% PEG MME 5000, 0.8 M K/Na tartrate, and 0.1 M Tris-HCl (pH 8.5)]. Phosphate ion-bound crystals were obtained via the sitting-drop method from a solution containing 15 mg/mL protein mixed with an equal volume of reservoir solution [1.0 M Na<sub>2</sub>HPO<sub>4</sub>/K<sub>2</sub>HPO<sub>4</sub> (pH 8.2)]. Diffraction quality crystals typically appeared within 3 days. The crystals were mounted on CryoLoops (Hampton Research) and flash-cooled in liquid nitrogen. The cryoprotectant consisted of 15% glycerol for the IMP-containing



Table 1. Crystal and Data Collection Statistics<sup>a</sup>

	with P <sub>i</sub>	with IMP	with XMP
space group	I4	I4	I4
unit cell parameters (Å)	a = 123.03, c = 140.72	a = 122.52, c = 140.90	a = 123.25, c = 141.64
no. of residues/protein	511	511	511
no. of molecules/asymmetric unit	2	2	2
no. of SeMet molecules/asymmetric unit	17	17	17
wavelength (Å)	0.97940	0.97939	0.97918
resolution limit (Å)	2.60 (2.60–2.64)	2.38 (2.38–2.42)	2.65 (2.65–2.70)
no. of observed unique reflections	31165 (1554)	41552 (2105)	30553 (1502)
data completeness (%)	97.0 (98.4)	99.9 (100)	99.9 (100)
$\langle I/\sigma(I) \rangle$	10.6 (2.6)	12.9 (3.3)	10.4 (3.2)
redundancy	5.6 (5.6)	10.0 (9.6)	9.1 (9.2)
R <sub>merge</sub> <sup>b</sup>	0.095 (0.725)	0.070 (0.776)	0.094 (0.735)

<sup>a</sup>Numbers in parentheses are values for the highest-resolution bin. <sup>b</sup>R<sub>merge</sub> =  $\sum_{hkl} \sum_i |I_i(hkl) - \langle I(hkl) \rangle| / \sum_{hkl} \sum_i \langle I_i(hkl) \rangle$ , where  $I_i(hkl)$  is the intensity for the  $i$ th measurement of an equivalent reflection with indices  $h$ ,  $k$ , and  $l$ .

Table 2. Phasing and Structure Refinement Statistics<sup>a</sup>

	with P <sub>i</sub>	with IMP	with XMP
Phasing			
resolution range (Å)	37.0–2.65	38.7–2.50	39.0–2.65
phasing method	MR	SAD	MR
search model	chains A and B of 1ZFI	—	chains A and B of 1ZFI
figure of merit	—	0.301	—
phasing power	—	1.465	—
Refinement			
resolution range (Å)	37.00–2.65	38.70–2.38	39.00–2.65
no. of reflections	31065	40903	29052
$\sigma$ cutoff	0.0	0.0	0.0
R <sub>work</sub>	0.184	0.172	0.195
R <sub>free</sub>	0.242	0.201	0.245
rmsd			
bond lengths (Å)	0.010	0.011	0.009
bond angles (deg)	1.32	1.41	1.28
dihedral angles (deg)	15.5	15.3	16.0
no. of protein residues	924	843	868
other molecules	124 H <sub>2</sub> O, 3 PO <sub>4</sub> <sup>3-</sup>	416 H <sub>2</sub> O, 2 IMP, 2 SO <sub>4</sub> <sup>2-</sup> , 4 glycerol, 1 Cl <sup>-</sup>	95 H <sub>2</sub> O, 2 XMP, 1 tartrate, 1 SO <sub>4</sub> <sup>2-</sup>
mean B factor (Å <sup>2</sup> )	61.4	41.6	82.7
Wilson B factor (Å <sup>2</sup> )	49.54	27.59	56.56
Ramachandran plot [most favored/outliers (%)]	94.9/0.1	98.3/0.0	95.7/0.0
PDB entry	3TSB	3USB	3TSD

<sup>a</sup>Because the structure of the protein–IMP complex was not available at the time when the structures of the phosphate ion-bound form and the complex with XMP were determined, the *S. pyogenes* structure (PDB entry 1ZFI) was used as an MR model for these two *B. anthracis* structures.

crystals and a saturated glucose solution in the crystal mother liquor for the P<sub>i</sub>- and XMP-containing crystals. Native and SeMet-labeled IMPDHs crystallized under similar conditions and diffracted X-rays from 2.38 to 2.65 Å.

**Data Collection, Structure Determination, and Refinement.** Diffraction data were collected at 100 K using the Q315r CCD detector (ADSC) at the 19-ID beamline of the Structural Biology Center at the Advanced Photon Source, Argonne National Laboratory.<sup>47</sup> For the crystal of IMPDH complexed with IMP, the three-wavelength inverse-beam multiwavelength anomalous dispersion (MAD) data sets from peak (0.97939 Å), inflection point (0.97930 Å), and high-energy remote (0.95385 Å) were collected from a single SeMet-labeled protein crystal (0.5 mm × 0.3 mm × 0.3 mm) to 2.38 Å resolution, with a 5 s exposure per 1° rotation frame and a 200 mm crystal–detector distance. The total rotation range was 180° on  $\omega$  as predicted using the strategy module in the HKL3000 suite. The inflection

data and the high-energy remote data were not included for the phasing because there was no contribution of data due to crystal decay. Thus, only peak 0.97939 Å was utilized. Similarly, the crystal data for the P<sub>i</sub>-bound complex and the IMPDH–XMP complex were collected at the same beamline. The single-wavelength data for the P<sub>i</sub>-bound form were collected to 2.6 Å at the 0.97940 Å value covering 130° (on  $\omega$ ), with a 7 s exposure and 1°/frame. For the IMPDH–XMP complex, 2.65 Å single-wavelength data at 0.97918 Å were obtained by collecting 220° (on  $\omega$ ) of diffraction images with a 5 s exposure and 1°/frame. All data were processed and scaled with HKL3000,<sup>48</sup> and the detailed crystal and data collection statistics are listed in Table 1.

The structure of the IMPDH–IMP complex was determined by SAD phasing with the peak data only up to 2.5 Å resolution using the HKL3000 software package.<sup>48</sup> selenium sites were determined by SHELXC<sup>49</sup> and SHELXD, the handedness was

checked by SHELXE,<sup>49</sup> phasing was done by MLPHARE,<sup>50</sup> density modification was done by DM,<sup>51</sup> and the initial model was built by ARP/wARP,<sup>52</sup> which contained 90% of the total of 1022 expected protein residues of the dimer. The initial model was further extended manually using COOT.<sup>53</sup> Cycles of manual adjustment of the model using COOT and REFMAC (CCP4 suite)<sup>54</sup> and PHENIX<sup>55</sup> refinement against the averaged peak data converged the model to the final  $R_{\text{work}}$  of 0.170 and the  $R_{\text{free}}$  of 0.201 with zero  $\sigma$  cutoff (Table 2). The structures of the phosphate ion-bound form of IMPDH and the IMPDH–XMP complex were determined by molecular replacement using MOLREP<sup>56</sup> on HKL3000. After the molecular replacement with chain A of the structure of IMPDH from *S. pyogenes* [Protein Data Bank (PDB) entry 1ZFJ, 69% identical sequence] as a search model to find a dimer, multiple cycles of both rigid-body refinement and restrained refinement were conducted with REFMAC.<sup>56</sup> This molecular replacement-produced model with the *S. pyogenes* protein (PDB entry 1ZFJ) sequence was then applied to AutoBuild routine on PHENIX<sup>55</sup> to rebuild in an effort to reduce a model bias and to correct the sequence (from *S. pyogenes* to *B. anthracis* IMPDH). Several alternating runs of PHENIX and manual adjustment using COOT further refined the resulting models, both for the phosphate ion-bound form and for the XMP complex. The final P<sub>i</sub>-bound structure contains 490 residues (from 511 residues, including uncleaved His<sub>6</sub> tag residues) for chain A and 434 residues for chain B with  $R_{\text{work}}$  and  $R_{\text{free}}$  values of 0.181 and 0.242, respectively (Table 2). The final IMPDH–XMP structures with 442 residues for chain A and 426 residues for chain B were converged to  $R_{\text{work}}$  and  $R_{\text{free}}$  values of 0.195 and 0.245, respectively. Both structures, except for approximately half of the CBS domain (residues 94–202), which is partly disordered, overall were well-defined. Native and SeMet-labeled IMPDHs have virtually identical structures.

The stereochemistry of all three structures was checked with PROCHECK<sup>57</sup> and MolProbity.<sup>58</sup> Final refinement statistics are listed in Table 2. All figures were prepared using PyMOL (W. L. DeLano, *The PyMOL Molecular Graphics System*, <http://www.pymol.org>).

**Enzyme Assays.** In all kinetic studies, the His<sub>6</sub>-tagged fusion or biotin-His<sub>6</sub>-tagged fusion constructs of native recombinant IMPDHs were used. When compared with that of the native enzyme, the activity of the SeMet-labeled *B. anthracis* enzyme was reduced 2-fold (data not shown). The concentration of the IMPDH fusion constructs was determined by absorbance at 280 nm using an extinction coefficient calculated by the ExPASy ProtParam tool. Except where noted, kinetic studies were performed in an assay buffer [50 mM Tris-HCl (pH 8.0), 100 mM KCl, 3 mM EDTA, and 1 mM DTT] containing varied concentrations of IMP and NAD<sup>+</sup> at 25 °C. Reactions were initiated by the addition of IMPDH to a final concentration of 50 nM. The production of NADH was measured by monitoring the increase in absorbance at 340 nm ( $\epsilon = 6.22 \text{ mM}^{-1} \text{ cm}^{-1}$ ) using a Shimadzu BioSpec-1601, Hitachi U-2000, or Cary 100 Bio spectrophotometer. All IMPDH preparations were shown to be free of contaminating NADH oxidase activity; this was verified with an assay buffer containing 50  $\mu\text{M}$  NADH. No oxidation of NADH was observed during the 40 min incubation period (data not shown). The pH dependence of the *B. anthracis* enzyme was determined in an assay buffer prepared with MES (pH 5.2–7.2), Tris-HCl (pH 7.2–9.0), or glycine (pH 8.6–10). Monovalent cation dependence was determined in an assay

buffer in which KCl was substituted with 100 mM NH<sub>4</sub>Cl, LiCl, CsCl, or NaCl. Kinetic parameters were determined by collecting initial velocity data at varying concentrations of IMP (5–1000  $\mu\text{M}$ ) and NAD<sup>+</sup> (100–8000  $\mu\text{M}$ ). For analysis of the steady state kinetic data for IMPDH enzymes displaying strong substrate inhibition with respect to NAD<sup>+</sup>, the method described by Kerr et al. was used.<sup>3,59</sup> First, kinetic parameters with respect to NAD<sup>+</sup> were obtained by plotting the initial velocity versus IMP at fixed NAD<sup>+</sup> concentrations and fitting the data to the Michaelis–Menten equation (eq 1). Apparent  $V_{\text{max}}$  values were then plotted versus NAD<sup>+</sup> concentration and fit to the uncompetitive substrate inhibition equation (eq 2). This yielded  $k_{\text{cat}}$ ,  $K_{\text{m}}$ , and  $K_{\text{ii}}$  values for NAD<sup>+</sup>. The  $K_{\text{m}}$  and  $k_{\text{cat}}$  for IMP were obtained by plotting the initial velocity versus NAD<sup>+</sup> at fixed IMP concentrations, fitting to eq 2, and then plotting the apparent  $V_{\text{max}}$  versus IMP concentration and fitting to eq 1. The  $k_{\text{cat}}$  values, identical within error, were averaged. Prism 4 (GraphPad Software) or SigmaPlot (SPSS, Inc.) was used for data analysis.

$$v = VA/(K_A + A) \quad (1)$$

$$v = (VB)/[K_B + B(1 + B/K_{\text{ii}})] \quad (2)$$

where  $v$  is the initial velocity,  $V$  is the maximal velocity,  $A$  and  $B$  are substrate concentrations,  $K_A$  and  $K_B$  are the respective Michaelis constants, and  $K_{\text{ii}}$  is the substrate inhibition constant for NAD<sup>+</sup>. Inclusion of a biotin tag at the N-terminus of the examined proteins had no significant effect on enzymatic activity.

**Inhibitor Kinetics.** Inhibition constants for XMP, MPA, A110, and C91 were determined with varying concentrations of IMP, XMP, and NAD<sup>+</sup> as indicated. Stock solutions of MPA, A110, and C91 were prepared in DMSO, and the final reaction concentration of DMSO was 5%. Because small amounts of DMSO (up to 15–20%) increased IMP dehydrogenase activity, control reactions for MPA experiments included 5% DMSO. Initial velocity data were fit to the equations for competitive inhibition

$$v = (VS)/[K_{\text{m}}(1 + I/K_{\text{is}}) + S] \quad (3)$$

noncompetitive inhibition

$$v = (VS)/[K_{\text{m}}(1 + I/K_{\text{is}}) + S(1 + I/K_{\text{ii}})] \quad (4)$$

and uncompetitive inhibition

$$v = (VS)/[K_{\text{m}} + S(1 + I/K_{\text{ii}})] \quad (5)$$

where  $S$  is the concentration of the varied substrate,  $I$  is the inhibitor concentration,  $K_{\text{m}}$  is the Michaelis constant, and  $K_{\text{is}}$  and  $K_{\text{ii}}$  are the slope and intercept inhibition constants, respectively. Global curve fits of the data were performed with Prism 4, and the  $F$  test was used to compare models.

**Determination of IC<sub>50</sub>.** Enzyme inhibition was assessed by monitoring the production of NADH by absorbance at varying inhibitor concentrations (50 pM to 10  $\mu\text{M}$ ). Each enzyme was incubated with an inhibitor for 10 min at room temperature prior to the addition of substrates. The following buffer conditions were used: 50 mM Tris-HCl (pH 8), 100 mM KCl, 1 mM DTT, 3 mM EDTA, 10 nM enzyme, and 1 mM IMP. Each enzyme required a different concentration of NAD<sup>+</sup>; generally  $\sim 2.5K_{\text{m}}$  (NAD<sup>+</sup>) was used as the NAD<sup>+</sup> concentration. IC<sub>50</sub> values were calculated for each inhibitor according to eq 6 using SigmaPlot (SPSS, Inc.)

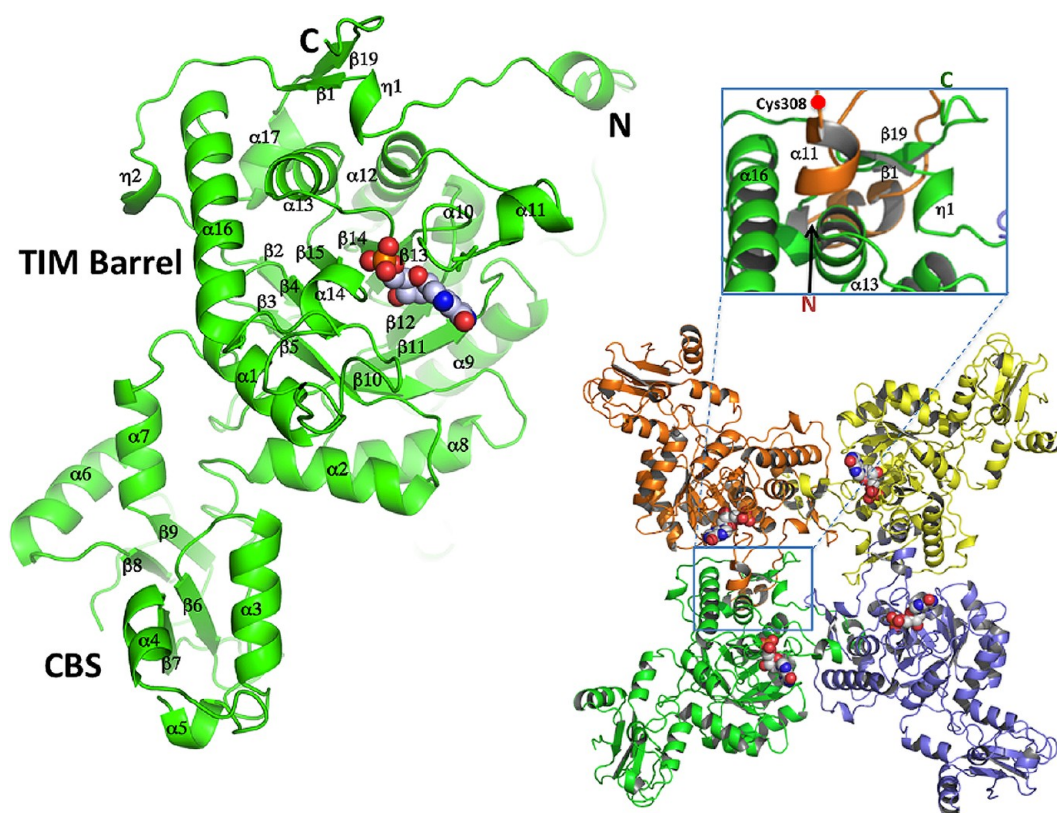


**Figure 3.** Structure of chain A of the *B. anthracis* IMPDH complex with IMP (gray space-filling model) showing the TIM barrel and CBS domains (left). Structure of the tetramer in a view parallel to the 4-fold axis (right). The tetramer was generated by performing the appropriate symmetry operation on the more complete monomer (chain A). Each subunit is shown in a different color with a space-filling model of IMP in the active site of each subunit. The inset above the tetramer shows the specific regions of the protein participating in the formation of the tetramer.

$$v_i = v_0 / (1 + I/IC_{50}) \quad (6)$$

where  $v_i$  is the initial velocity in the presence of inhibitor I and  $v_0$  is the initial velocity in the absence of inhibitor.

**Inhibitor Binding Studies.** Analysis of the binding of inhibitors to IMPDH proteins was performed using biolayer interferometry (BLI)<sup>60</sup> on the Octet RED (ForteBio, Menlo Park, CA). Assays were performed in 96-well black microplates (Fisher Scientific, Pittsburgh, PA) at 25 °C. All volumes were 300  $\mu$ L. Biotinylated IMPDH was loaded onto Super Streptavidin (SSA) Biosensors (ForteBio) at a concentration of 50  $\mu$ g/mL in phosphate-buffered saline (PBS). Reference SSA Biosensors were blocked with biocytin at 10  $\mu$ g/mL in PBS buffer. Each tested inhibitor was titrated from 0.2 nM to 10  $\mu$ M (a concentration of up to 30  $\mu$ M was tested for the *V. cholerae* enzyme) in a buffer containing 50 mM Tris-HCl (pH 8), 100 mM KCl, 1 mM DTT, 3 mM EDTA, 0.1 mg/mL BSA, 5% DMSO, 1 mM IMP, and NAD<sup>+</sup> in specific amounts for a given enzyme. Assays were run first using the protein biosensors, followed by the reference biosensors using the same protocol. The reference data were then subtracted from the protein data. The association and dissociation curves were fit using a single-exponential fitting model using analysis software provided by the manufacturer.

**Coordinates.** The atomic coordinates for the P<sub>i</sub>, IMP-, and XMP-bound structures of *B. anthracis* IMPDH have been deposited in the PDB as entries 3TSB, 3USB, and 3TSD, respectively.

## RESULTS

**Overall Structure of IMPDH from *B. anthracis*.** We have determined three crystal structures of *B. anthracis* IMPDH, a phosphate ion-bound form (an apo form), in complex with the substrate, IMP, and in complex with the product, XMP. Both IMP- and XMP-containing structures were obtained by cocrystallization. The phosphate ion present in the active site of the apo form most likely originated from the crystallization buffer. The IMP-bound structure was determined by single-wavelength anomalous diffraction (SAD) phasing using the HKL3000 software package.<sup>48</sup> The structures of the phosphate ion- and XMP-containing IMPDH were determined by molecular replacement.

Size exclusion chromatography shows that *B. anthracis* IMPDH exists as a homotetramer in solution (Figure S1 of the Supporting Information), and it crystallizes as such. All three structures contain two monomers in the asymmetric unit. The *B. anthracis* IMPDH monomer has a typical two-domain structure, the catalytic domain, which is a TIM barrel, and the CBS domain (Figure 3). In all structures reported here, each monomer contains a ligand bound in the active site (phosphate anion in the apo structure and IMP and XMP in the substrate- and product-bound structures, respectively). In all the structures, the CBS domains are partially disordered.

The tetrameric structure of IMPDH is stabilized by intermonomer contacts with each of the adjacent subunits. The C-terminus is close ( $\sim 15$  Å) to the catalytic site and on the opposite face of the tetramer from the N-terminus. In the tetramer, all C-termini are close to each other ( $\sim 12$  Å). The subunit interactions can be categorized into three groups



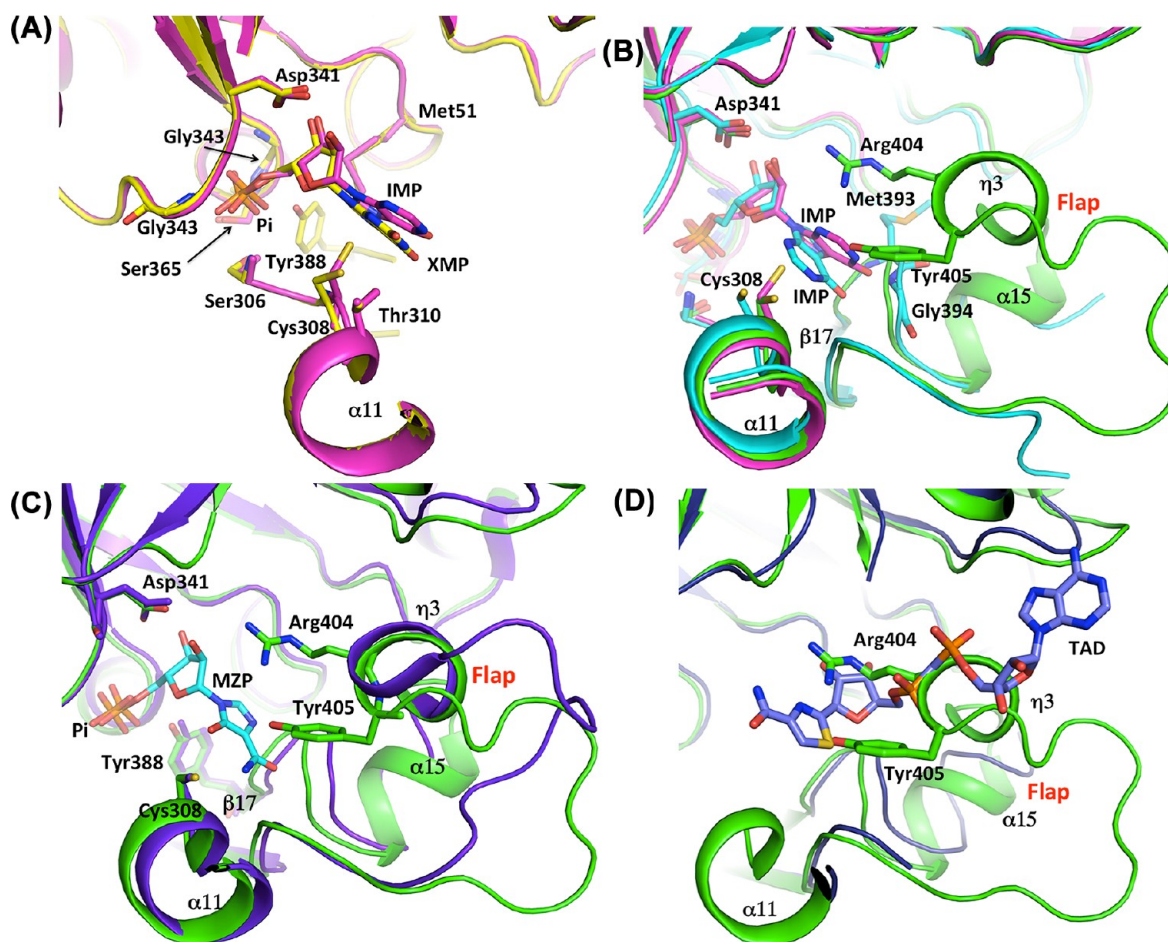


**Figure 4.** Structural alignment of IMPDH active sites. (A) Overlap of the *B. anthracis* IMPDH structures of  $P_i$  (green), IMP (magenta), and XMP (yellow) complexes showing the positions of the IMP and XMP (magenta and yellow sticks, respectively). (B) Overlap of the *B. anthracis*  $P_i$ -bound (green) and IMP-bound (magenta) structures with the *S. pyogenes* enzyme-IMP complex (PDB entry 1ZFJ) (turquoise). IMP molecules (*B. anthracis* in magenta, *S. pyogenes* in turquoise) are depicted as sticks. *S. pyogenes* residues Met393 and Gly394 interacting with IMP are also depicted as sticks. (C) Overlap of the structures of the *B. anthracis*  $P_i$ -bound enzyme (green) with the *T. foetus* IMPDH complex with MZP (purple) (PDB entry 1PVN<sup>20</sup>). The conserved Arg-Tyr dyad within helix  $\eta_3$  of the flap is depicted as sticks. (D) Overlap of the structures of the *B. anthracis*  $P_i$ -bound enzyme (green) with the *T. foetus* IMPDH (purple) complex with IMP (omitted for the sake of clarity) and TAD (purple) (PDB entry 1LRT<sup>19</sup>). A distal portion of the *B. anthracis* catalytic flap with the conserved Arg-Tyr dyad is clashing with the *T. foetus*  $\beta$ -methylene-thiazole portion of TAD, indicating that these two elements are occupying the same space within the active site.

depending on their proximity to the catalytic site and level of amino acid sequence conservation. In one group, the first 14 residues of the N-terminus (including  $3_{10}$ -helix,  $\eta_1$ ) project approximately 20 Å from the TIM barrel (Figure 3) and interact with surface residues of an adjacent IMPDH monomer. This regional contact is distal from the catalytic site and involves residues 3–12 of the N-terminus that interact with  $\beta$ -sheet ( $\beta_{19}$ ) residues 460–463 of an adjacent subunit. The interaction involves hydrogen bonds and salt bridges between residues that display little sequence conservation. Another loop (residues 18–27) and  $3_{10}$ -helix  $\eta_2$  are involved in subunit contacts with the adjacent IMPDH molecule and also form part of the active site pocket of the adjacent subunit. Additional subunit contacts originate from helix  $\alpha_{11}$  (residues 310–315) and a loop (residues 316–319), interacting with  $\beta$ -sheet  $\beta_1$  (residues 16–19) and residues 479–484 in an adjacent IMPDH monomer. These regions are approximately 20 Å from the substrate-binding site.

The catalytic domain (residues 1–90 and 222–487) forms the core of the tetramer and is approximately 40 Å × 40 Å × 50 Å. This domain is a classic eight-fold  $\beta/\alpha$  TIM barrel with the

active site loop (residues 302–329) containing catalytic Cys308 positioned on the proximal face of the  $\beta/\alpha$ -barrel near the subunit interface (Figure 3). The CBS domain is composed of tandem motifs (residues 91–221, approximately 20 Å × 20 Å × 40 Å) and projects outward from the tetramer. Of the two monomers in the asymmetric unit, molecule A in the phosphate ion-bound structure has the most complete electron density for the CBS domain. In the IMP-containing structure determined at higher resolution (2.38 Å), four residues are missing in the loop connecting the tandem CBS motifs and 12 residues are missing in the structure with XMP. The structure of *B. anthracis* IMPDH is most similar to that of IMPDH from *S. pyogenes* (PDB entry 1ZFJ).<sup>15</sup> Alignment of these structures using the SSM server of the European Bioinformatics Institute (<http://www.ebi.ac.uk/msd-srv/ssm>)<sup>61</sup> yielded a backbone rmsd of 1.34 Å and 69% sequence identity. In addition to the *S. pyogenes* enzyme, there are four other structures of microbial IMPDHs available in the PDB. These include IMPDHs from *Thermotoga maritima* [PDB entry 1VRD, 60% sequence identity, 1.03 Å rmsd (DOI 10.2210/pdb1vrd/pdb)], *C. parvum* (PDB entry 3FFS, 57% sequence identity, 1.03 Å rmsd<sup>22</sup>), *Bo. burgdorferi*



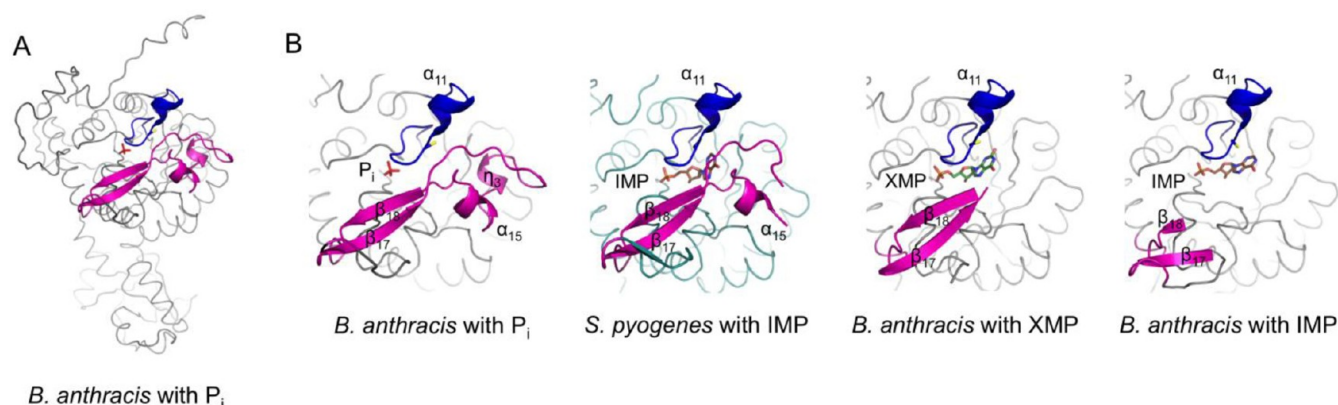


**Figure 5.** Different degrees of flap disorder in bacterial IMPDHs. (A) *B. anthracis* monomer (molecule A) of the highly ordered  $P_i$ -bound (apo) structure. (B) Detail of the active site, from left to right, of the *B. anthracis*  $P_i$ -bound enzyme (entire flap ordered), the *S. pyogenes* complex with IMP (missing residues 402–415 that include helix  $\eta_3$ ), and the *B. anthracis* complex with XMP (missing residues 394–414, including helices  $\alpha_{15}$  and  $\eta_3$ ) and with IMP (missing residues 381–421), respectively. The catalytic flap is colored magenta, and the catalytic loop is colored dark blue, with the catalytic Cys represented as sticks. Ligands ( $P_i$ , IMP, and XMP) are colored red, orange, and green sticks, respectively.

(PDB entry 1EEP, 55% sequence identity, 0.96 Å rmsd<sup>17</sup>), and *Pyrococcus horikoshii* [PDB entry 2CU0, 50% sequence identity, 1.04 Å rmsd (DOI 10.2210/pdb2cu0/pdb)]. All of these enzymes show similar structural features and active sites.

**Substrate and Product Binding.** IMP dehydrogenase catalyzes the oxidation of IMP to XMP with the concomitant reduction of  $NAD^+$  to NADH. During the reaction, IMP forms a covalent adduct with the active site Cys residue (Cys308 in *B. anthracis*), the hydride ion is transferred from the C2 atom of the hypoxanthine ring to  $NAD^+$ , and the oxygen atom is placed in this position resulting in the formation of xanthosine. In the structures of *B. anthracis* IMPDH with IMP and XMP, the substrate or product is bound in a pocket located inside the  $\beta$ -barrel structure. Binding of these ligands is characterized by subtle conformational changes. In both structures, the ribose and phosphate moieties assume virtually identical conformations and are highly coordinated by the protein. The sugar moiety is in the C2'-endo conformation, and its 2'- and 3'-hydroxyl groups are hydrogen-bonded with Asp341. The phosphate group is anchored by a number of amino acid side chains (Ser306, Ser365, and Tyr388; surprisingly, Tyr388 is ordered in the XMP-bound structure but is disordered when IMP is bound) and three main chain nitrogen atoms (Gly343, Gly364, and Ser365) (Figure 4A). The remaining hydrogen bonding potential of the phosphate oxygen atoms is fulfilled by water molecules. The conformation of the purine ring is somewhat different in the two liganded structures. In the structure with IMP, the Cys308 sulfur atom is located 3.5 Å (chain A) and 3.9 Å (chain B) from the C2 atom of the inosine ring and is not covalently linked to the ring. This conformation of inosine seems to be stabilized by the side chains of Ile307, Cys308, and Met51. In the XMP-bound structure, the xanthosine ring is rotated (rotation defined on the basis of the O4–C1'–N9–C4 torsion angle within the IMP and XMP molecule) by  $\sim 10^\circ$  (the difference between the chain A/B-averaged torsion angle for each ligand) with respect to the position of the inosine ring and its C2 atom is closer (3.4 and 3.7 Å for chains A and B, respectively) to the sulfur of Cys308 (Figure 4A). This conformation is typically observed in other XMP-IMPDH complexes<sup>21</sup> and causes the Cys308 side chain to rotate away from the XMP molecule. The hydroxyl group of Thr310 forms a hydrogen bonding interaction with the O2 atom of XMP. In the structure of the apoenzyme, the

phosphate anion occupies the same position as the IMP or XMP phosphate group and makes the same contacts with the protein that are observed for the phosphate moiety in the structures with IMP and XMP. These include interactions with amino acid side chains of Ser306, Ser365, and Tyr388 and three main chain nitrogen atoms of Gly343, Gly364, and Ser365. In contrast to the *Trichomonas foetus* IMPDH,<sup>21</sup> in all three structures of the *B. anthracis* IMPDH the catalytic loop containing Cys308 is ordered and exhibits very little conformational dynamics (Figure 4A,B). Although potassium chloride was included in the crystallization medium, electron density for a potassium ion was not observed in any of our structures (the metal ion position is occupied by water molecules in our structures).

**Active Site Flap.** After the hydride transfer, the E-XMP\* intermediate is covalently trapped in the active site and the Cys308–XMP\* bond must be hydrolyzed for the product to be released. The active site flap is a mobile element containing the catalytic dyad (Arg404 and Tyr405), which positions itself into the active site during the hydrolysis phase of the reaction. This flap shows a varying degree of disorder in reported structures. The structure of the complete flap has been captured only for the *T. foetus* IMPDH in the presence of the transition state analogue, mizoribine 5'-monophosphate (MZIP).<sup>20</sup> In the *B. anthracis* IMPDH structure with IMP, residues 381–421, which comprise most of the flap region, are disordered. A larger portion of the flap is visible in the structure with XMP, with only residues 394–414 missing. Interestingly, the entire flap is visible in the apo ( $P_i$ -bound) structure (Figure 5). Figure 4B shows a comparison of the three structures: the *B. anthracis* phosphate ion-bound enzyme, the *B. anthracis* enzyme in complex with IMP, and the *S. pyogenes* IMPDH–IMP complex, with a partially ordered active site flap. In the *S. pyogenes* structure, the base of the flap consists of a small, three-stranded antiparallel  $\beta$ -sheet ( $\beta_{16}$ – $\beta_{18}$ , the “finger domain”). A loop that extends from the second strand of the  $\beta$ -sheet ( $\beta_{17}$ ) is partially ordered and contains residues (*S. pyogenes* Met393 and Gly394) that contact the purine residue of IMP (Figure 4B). The distal portion of this loop, containing the catalytic Arg-Tyr dyad, is disordered in the *S. pyogenes* structure as it is in most other IMPDH structures but is visible in the structure of the apoenzyme. The portion of the loop ordered in the structure of the apoenzyme contains a small  $\alpha$ -helix ( $\alpha_{15}$ , residues 394–

399) followed by a  $3_{10}$ -helix ( $\eta_3$ , residues 401–405) (Figure 4B) and a longer loop (residues 406–416). The flap is ordered because several residues (side chains of Lys386, Arg389, Asp403, Arg404, Asn410, Glu416, and Lys425, main chain carbonyl, and amide groups of Gly400, Arg404, Glu419, Arg420, and Gly426) of this structural motif interact with the main body of the enzyme (both within the subunit and with the neighboring subunit). For example, the C-terminal sequence of the neighboring subunit forms a  $\beta$ -strand ( $\beta_{20}$ , residues 476–480) that complements the  $\beta$ -finger of the flap with Lys480 providing an additional bridging interaction with Glu419 of the flap. There are also interactions within the flap unit (for example, Lys402 and Gln407). Arg404 and Tyr405, located within the  $3_{10}$ -helix,  $\eta_3$ , extend toward the active site. The conformation of these residues is maintained through the bridging interaction with Asp251. An overlap of the *B. anthracis* phosphate ion-bound structure with the *T. foetus* structure of the MZP–enzyme complex (PDB entry 1PVN, rmsd on  $\text{Ca}$  atoms of compared 362 residues of 1.23 Å),<sup>20</sup> the only other structure with a completely ordered flap, shows that the active site flaps maintain remarkable structural similarity with only ~40% sequence identity (Figure 4C). Several conserved side chains assume virtually identical conformations [numbers in parentheses are in *T. foetus* notation, Tyr388 (405), Gly390 (407), Gly392 (409), Ser393 (410), Arg404 (418), Tyr405 (419), Glu416 (431), Gly417 (432), Pro423 (438), and Tyr424 (439)]. The only significant differences are observed in the loop regions of the flap. The small  $\alpha$ -helix ( $\alpha_{15}$ , residues 394–399) in the *B. anthracis* structure is replaced by a loop in the *T. foetus* structure (residues 411–414) (Figure 4C). Also, a portion of the loop (residues 406–414) connecting helix  $\eta_3$  and sheet  $\beta_{18}$  (residues 406–419) is shifted toward the center of the tetramer in the *B. anthracis* structure, whereas the corresponding portion of the *T. foetus* loop faces the other monomer (Figure 4C). Interesting information about the flap movement during catalysis can be obtained by comparing the *B. anthracis* apo structure with the structure of *T. foetus* IMPDH in complex with IMP and an  $\text{NAD}^+$  analogue,  $\beta$ -methylene-thiazole-4-carboxamide-adenine dinucleotide (TAD).<sup>20</sup> In that structure, the TAD molecule lies in the cleft between two adjacent monomers; the thiazole ring stacks against the inosine ring of IMP, and a portion of the flap is missing (*T. foetus* residues 417–429). An overlap of the *B. anthracis* apo ( $\text{P}_i$ -bound) structure with the *T. foetus* enzyme–IMP–TAD complex (PDB entry 1LRT, rmsd for  $\text{Ca}$  atoms of 338 compared residues of 1.23 Å) indicates that the conserved Arg–Tyr dyad (helix  $\eta_3$ ) occupies the nicotinamide subsite of  $\text{NAD}^+$  within the active site (Figure 4D). This observation suggests that the portion of the flap swings in and out of the  $\text{NAD}^+$  site during catalysis. Because the flap is disordered in all structures containing IMP and XMP, it suggests that binding of a ligand causes the flap to become disordered by disrupting the interaction of this structural motif with the main body of the enzyme. The conformation or ordering of the flap does not seem to depend on the crystal packing because the structures of *B. anthracis* IMPDHs are isomorphic. The flap environment is very similar in all *B. anthracis* structures, and the contacts made by the flap are mainly intramolecular with the adjacent monomer within the same tetramer. A possible explanation for the flap stability in the phosphate ion-bound enzyme is the presence of a small hydrophobic core near the active site. This core is formed by the flap (residues Tyr388, Ile418, and Val422), the active site loop (residues Ile307 and Thr309), and the loop from the

neighboring subunit (residues His471, Ile478, Tyr485, and Tyr346). Disruption of this core by binding of a ligand would clearly have a detrimental effect on the maintenance of the structure of the flap.

**Kinetic Characterization of *B. anthracis* IMPDH.** The kinetic properties of *B. anthracis* IMPDH are similar to those of other microbial IMPDH enzymes.<sup>15,62–64</sup> The enzyme has a pH optimum of 8.2 and a strict requirement for monovalent cation. Optimal activation occurs with  $\text{K}^+$  concentrations between 100 and 150 mM; however, inhibition is observed at higher concentrations. The enzyme shows  $\leq 1\%$  activity with 100 mM  $\text{Na}^+$  or  $\text{Li}^+$  or in the absence of monovalent cations; 100 mM  $\text{NH}_4^+$  or  $\text{Cs}^+$  yielded 77 or 36% activity, respectively, relative to the activity in the presence of 100 mM  $\text{K}^+$ , the typical assay concentration. Plots of initial velocity versus IMP concentration at fixed  $\text{NAD}^+$  concentrations are consistent with the Michaelis–Menten kinetics. Substrate inhibition was observed at high  $\text{NAD}^+$  concentrations (Figure 6B).<sup>3,65</sup>

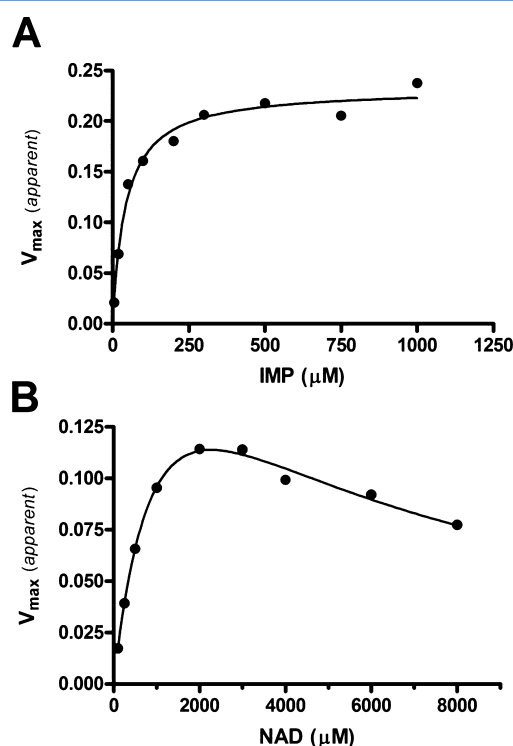


**Figure 6.** Steady state kinetics of *B. anthracis* IMPDH. (A) Secondary plot of kinetic data showing apparent  $V_{\max}$  values (from initial velocity vs  $\text{NAD}^+$  plots) plotted vs IMP concentration. The solid line represents the best fit to eq 1 for Michaelis–Menten kinetics. (B) Secondary plot of kinetic data showing apparent  $V_{\max}$  values (from initial velocity vs IMP plots) plotted vs  $\text{NAD}^+$  concentration. The solid line represents the best fit to eq 2 for uncompetitive substrate inhibition.

Secondary plots of the initial velocity versus IMP and  $\text{NAD}^+$  are shown in Figure 6, and the steady state parameters are listed in Table 3. XMP is a competitive inhibitor versus IMP. MPA displays noncompetitive inhibition versus IMP and  $\text{NAD}^+$  (Table 3). The Michaelis–Menten kinetic characterization was also performed for IMPDHs from three other bacterial species, *Ca. jejuni*, *Cl. perfringens*, and *V. cholerae*. All tested proteins exhibit similar  $K_m$  values for the substrate, IMP, and have requirements for higher  $\text{NAD}^+$  concentrations than eukaryotic enzymes (Table 4).

**Table 3. Kinetic Parameters for Inhibition of *B. anthracis* IMPDH by XMP and MPA**

inhibitor	vs IMP <sup>b</sup>	inhibition pattern <sup>a</sup>	K <sub>is</sub> (μM)	K <sub>ii</sub> (μM)
XMP	vs IMP <sup>b</sup>	C	218 ± 6	na <sup>c</sup>
MPA	vs IMP <sup>b</sup>	NC	na <sup>c</sup>	4.83 ± 0.04
MPA	vs NAD <sup>+</sup> <sup>d</sup>	NC	na <sup>c</sup>	3.9 ± 0.2

<sup>a</sup>C, competitive; NC, noncompetitive. <sup>b</sup>NAD<sup>+</sup> concentration fixed at 1.3 mM. <sup>c</sup>Not applicable. <sup>d</sup>IMP concentration fixed at 750 μM.

**Table 4. Kinetic Parameters of Bacterial IMPDH Proteins**

	<i>B. anthracis</i>	<i>Ca. jejuni</i>	<i>Cl. perfringens</i>	<i>V. cholerae</i>
k <sub>cat</sub> (s <sup>-1</sup> )	1.4 ± 0.2	2.2 ± 0.3	0.6 ± 0.1	2.1 ± 0.2
K <sub>m</sub> (IMP) (μM)	18 ± 2	25 ± 3	11 ± 2	80 ± 10
K <sub>m</sub> (NAD) (μM)	550 ± 50	220 ± 20	370 ± 4	1200 ± 200
K <sub>ii</sub> (NAD) (mM)	3.9 ± 0.5	20 ± 4	13 ± 2	na <sup>a</sup>

<sup>a</sup>Not applicable.

**IMPDH Inhibition.** *C. parvum* IMPDH-selective inhibitors have been recently identified in a high-throughput screen targeting the NAD<sup>+</sup>-binding site.<sup>22,39,40</sup> Because *B. anthracis* IMPDH contains the Ala253-Tyr445 (*C. parvum* Ala165-Tyr358) structural motif that defines the susceptibility of the enzyme to *C. parvum* inhibitors, the *B. anthracis* enzyme should also be sensitive to these inhibitors. To test this hypothesis, IC<sub>50</sub> data for the *B. anthracis* IMPDH were measured for two of the *C. parvum* inhibitors, a quinolinium-substituted triazole derivative, A110,<sup>41</sup> and a 2-pyridinyl derivative of benzimidazole, C91<sup>38</sup> (Figure 7). To compare the inhibition properties of A110 and C91 for other bacterial enzymes, we also obtained IC<sub>50</sub> values for IMPDHs from *Ca. jejuni*, *Cl. perfringens*, and *V. cholerae*. Because *V. cholerae* IMPDH does not contain the Ala165-Tyr358 structural motif, a much lower affinity for A110 and C91 was expected and the *V. cholerae* enzyme was used as a negative control. The *B. anthracis* and *Ca. jejuni* enzymes exhibited similar sensitivities to A110 and C91 (IC<sub>50</sub> values in the range of 51–120 nM), whereas *Cl. perfringens* IMPDH was generally less sensitive to both inhibitors, with 2- and 10-fold larger IC<sub>50</sub> values for A110 (280 ± 30 nM) and C91 (570 ± 20 nM), respectively (Table 5).

In addition, to test an alternative to a typical kinetic assay, biolayer interferometry (BLI)<sup>60</sup> was utilized to determine the apparent dissociation constant, K<sub>D</sub>, for binding of the inhibitors to IMPDHs. The relationship of IC<sub>50</sub> to K<sub>i</sub> (K<sub>D</sub> values in BLI) is described by Cheng and Prusoff.<sup>66</sup> This relationship depends on substrate concentration [S], the reaction mechanism, and the inhibitor's mode of inhibition. In the case of competitive inhibition, IC<sub>50</sub> values approximate K<sub>D</sub> when the [S] used in the assay is much lower than K<sub>m</sub>. For uncompetitive inhibition, IC<sub>50</sub> values approximate K<sub>D</sub> when the [S] in the assay is much higher than K<sub>m</sub>. For noncompetitive (mixed) inhibition, IC<sub>50</sub> does not depend on [S] and will be equal to K<sub>D</sub>.<sup>67</sup> This last mode of inhibition applies to the case of IMPDH inhibition

presented here. BLI is a label-free technology for measuring biomolecular interactions. It is an optical technique that analyzes the interference pattern reflected from two surfaces: a layer of the immobilized protein on a biosensor tip and the reference layer. The binding between an immobilized protein and a ligand in solution produces the increase in optical thickness at the biosensor tip, which causes a shift in the interference pattern that can be measured in real time.<sup>60,68</sup> Binding affinities of A110 and C91 for *B. anthracis*, *Ca. jejuni*, *Cl. perfringens*, and *V. cholerae* IMPDHs were measured using BLI (Figure 7). A comparison of IC<sub>50</sub> values and K<sub>D</sub> is

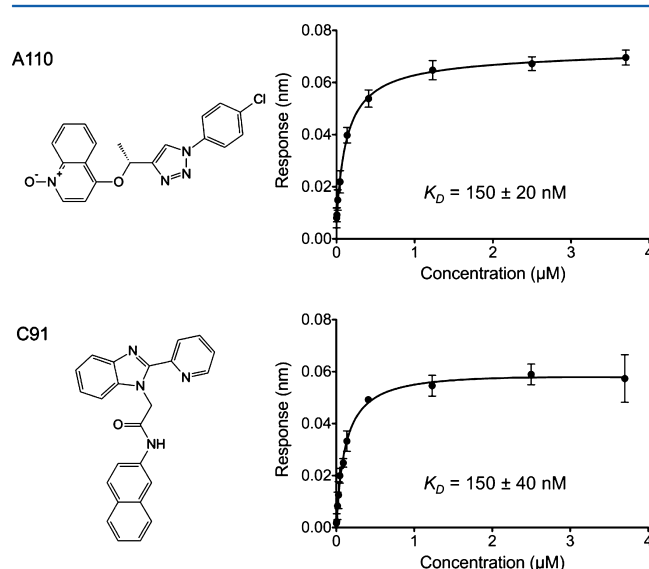


**Figure 7.** Biolayer interferometry analysis using Octet RED of binding of A110 and C91 to *B. anthracis* IMPDH. The analysis was performed in triplicate. For each triplicate, the responses were fit to a 1:1 protein–ligand interaction model. The obtained values were used to generate steady state plots.

presented in Table 5. The values for K<sub>D</sub> obtained using BLI agree within 3-fold with the IC<sub>50</sub> values obtained spectrometrically. Generally, regardless of the mode of inhibition, IC<sub>50</sub> values are expected to be higher or equal to K<sub>D</sub> values. All K<sub>D</sub> values listed in Table 5 are higher than the corresponding IC<sub>50</sub> values, but they agree within 3-fold (i.e., 57 ± 7 nM vs 150 ± 20 nM). This correlation is considered to be within the experimental error, given the two vastly different experimental designs.<sup>69</sup>

## DISCUSSION

**Overall Structure of Bacterial IMPDHs.** All IMPDH enzymes share several common characteristics. The active form of the enzyme is a tetramer with four active sites per oligomer. The reaction proceeds through several distinct steps. IMPDH enzymes have an active site cysteine residue that upon IMP binding forms a covalent intermediate. Here we were able to

**Table 5. Inhibition of IMPDHs by Compounds A110 and C91**

	<i>B. anthracis</i>		<i>Ca. jejuni</i>		<i>Cl. perfringens</i>		<i>V. cholerae</i>	
	IC <sub>50</sub> (nM)	K <sub>D</sub> (nM)	IC <sub>50</sub> (nM)	K <sub>D</sub> (nM)	IC <sub>50</sub> (nM)	K <sub>D</sub> (nM)	IC <sub>50</sub> (nM)	K <sub>D</sub> (nM)
A110	57 ± 7	150 ± 20	120 ± 20	200 ± 18	280 ± 30	490 ± 42	>5000 <sup>a</sup>	>5000
C91	57 ± 1	150 ± 40	51 ± 9	140 ± 10	570 ± 20	1100 ± 62	>5000 <sup>a</sup>	>5000

<sup>a</sup>Concentrations of >5 μM were not tested.



capture the *B. anthracis* IMPDH in three different states. A substrate-bound form shows that IMP is anchored in the active site using the phosphosugar moiety. The inosine ring remains quite flexible, and on the basis of our structures and those previously reported, it assumes at least two distinct conformations. The *B. anthracis* IMPDH product-bound state is very similar to all structures reported to date. In both of these forms, the active site flap is mostly disordered. The third structure is of an apoenzyme, which contains a phosphate ion bound in the active site (corresponds to the position of a phosphate group in IMP and XMP). In this structure, the active site flap is fully ordered and its conformation is consistent with the role of Arg404 and Tyr405 as the catalytic dyad during the hydrolysis step.

A consensus sequence that includes an active site cysteine has been proposed as a signature motif for the IMPDHs as well as GMP reductase enzymes. Alignment of these consensus sequences of bacterial and eukaryotic IMPDH enzymes shows a significant conservation with 30–40% sequence identity among organisms. However, regions that lack homology on the basis of a global comparison show similarity when the comparison is restricted to the bacterial or eukaryotic group. In this restricted comparison, 90% of the residues are conserved in this region of the active site for either the bacterial or eukaryotic group.<sup>32</sup> The availability of structural information for several IMPDH enzymes provides a resource for defining the distinct characteristics of bacterial and eukaryotic enzymes. Features such as the catalytic pocket, catalytic loop, and flap are conserved, but some distinct characteristics have been identified for bacterial IMPDHs. These discriminatory signatures of bacterial and mammalian IMPDH enzymes can be exploited in the development of bacterium-specific inhibitors. For example, the presence of the Ala165-Tyr358 structural motif defines the susceptibility of the enzyme to *C. parvum* inhibitors.

Currently, there are 26 structures of IMPDHs deposited in the PDB, only seven of which (including three *B. anthracis* structures presented here) are from bacteria and one of which is from archaea. The best structurally characterized is the IMPDH from *T. foetus* for which several structures with substrate, cofactor, MPA, transition state analogue MZP, and ribavirin 5'-monophosphate (RMP) have been determined. However, there is still the need for more comprehensive structural characterization of bacterial enzymes, which would offer valuable insights into the mechanistic specifics of prokaryotic IMPDHs. Three crystal structures of the *B. anthracis* IMPDH presented here provide an important contribution in the process of elucidation of the bacterial IMPDH signature.

**Catalytic Site and Implications for the Mechanism of Bacterial IMPDH.** Covalent tetrahedral intermediate formation has been proposed.<sup>70</sup> However, our structures show that IMPDH does not form a covalent bond with the substrate in the absence of the NAD<sup>+</sup> cofactor. Therefore, the cofactor not only plays the role of hydride acceptor but also completes the structure of the catalytic pocket. Initiation of the reaction cycle requires alignment of inosine and nicotinamide rings in near parallel fashion and positioning of the C2 atom of the inosine ring close to the C4 atom on the *pro-S* face of the nicotinamide ring.<sup>27,71</sup> It appears that only then can the formation of thioimide occur. This mechanism is in striking contrast with results obtained with halogenated derivatives of IMP. IMPDH catalyzes the dehalogenation of 2-fluoro- and 2-chloro-inosine 5'-monophosphate in the absence of NAD<sup>+</sup>.<sup>72</sup> This suggests that the Cys308 activation system is in place, but the reaction

does not proceed with IMP alone because the hydride is a poorer leaving group than chloride and fluoride. However, the inosine ring seems to exist in multiple conformations, some of which may result in a productive covalent adduct, providing a suitable leaving group is present. For IMP, the NAD<sup>+</sup> cofactor is required to position the inosine ring for the Cys308 attack and the subsequent transfer of hydride. In the structure of the hamster IMPDH (PDB entry 1JR1), which also contains a molecule of MPA in the active site, the inosine ring is covalently attached to Cys331 (equivalent to Cys308 in our structure). The hamster IMPDH structure represents the covalent thioimide (E-XMP\*) intermediate of the reaction, in which MPA, an uncompetitive inhibitor, prevents the hydrolysis of the thiopurine intermediate by the catalytic dyad (Arg404 and Tyr405) as was originally suggested by Link and Straub.<sup>34</sup>

Unlike previous structures, with the exception of the *T. foetus* enzyme complex with MZP,<sup>20</sup> the entire flap is well-ordered in the structure of the *B. anthracis* phosphate ion-bound enzyme. The distal portion of the flap folds into the active site, creating a closed conformation. This closed conformation is stabilized by the interactions of several residues of this structural motif with the main body of the enzyme. Binding of IMP or XMP disrupts these interactions and forces the flap to move away from the active site. This is signified by the disorder of portions of the flap in the structure of substrate and product complexes. This may indicate that for the *B. anthracis* enzyme, the equilibrium between the open and closed conformation is shifted toward the closed conformation in the absence of IMP and/or NAD<sup>+</sup>. Binding of the substrate appears to induce the open conformation.

Although potassium chloride was included in the crystallization medium, electron density for a potassium ion was not observed in any of our structures. To date, only five (of 26 deposited) X-ray crystal structures of IMPDHs identified a conserved metal (K<sup>+</sup> or Na<sup>+</sup>) binding site near the loop containing the catalytic Cys residue. K<sup>+</sup> ion has been observed in the structures of the Chinese hamster E-XMP\*-MPA complex (PDB entry 1JR1)<sup>13</sup> and IMP analogue complexes, human type II E-RVP-MAD [PDB entry 1NF7 (DOI 10.2210/pdb1nf7/pdb)] and *T. foetus* E-MZP (PDB entry 1PVN).<sup>20</sup> Na<sup>+</sup> ion was located at the same site in the structures of *T. foetus* E-RVP (PDB entry 1ME8) and E-RVP-MPA (PDB entry 1ME7).<sup>18</sup> In the case of K<sup>+</sup> ion, its binding site is formed by six main chain carbonyls from two adjacent monomers. For *T. foetus*, these include three carbonyls from the Cys319 loop (Gly314, Gly316, and Cys319) and three from an  $\alpha$ -helix in the C-terminal portion of the adjacent subunit (Glu485, Gly486, and Gly487).<sup>18,20</sup> A second potassium site is observed exclusively in *T. foetus* IMPDH. This site is also located at the interface of two monomers and involves interactions with residues that are not conserved in *B. anthracis* or any other organism.<sup>18,19</sup> The metal binding site associated with the active site Cys-containing loop is thought to be catalytically important. This site is disrupted in many structures that are believed to reflect intermediate stages of the catalytic cycle, suggesting that K<sup>+</sup> binds only to the specific state of the enzyme, such as E-XMP\*.<sup>13,20</sup> However, it was recently shown through biochemical experiments and molecular dynamics simulations that K<sup>+</sup> is present throughout the catalytic cycle but plays a major role in influencing the rate of the catalytic flap closure. Specifically, the presence of K<sup>+</sup> is proposed to decrease the activation barrier for the flap movement by providing an alternative orientation (or disruption) of the Cys loop and thus

facilitating the interaction between the loop and the flap, allowing flap closure.<sup>73</sup> Interestingly, *T. foetus* IMPDH is also activated by Na<sup>+</sup> and thus it is not K<sup>+</sup>-specific. This lack of ion specificity is thought to be associated with a higher flexibility of the catalytic loop that is observed for *T. foetus*.<sup>3</sup> This flexibility is not seen in the *B. anthracis* enzyme or any other K<sup>+</sup>-specific IMPDHs such as that of *Bo. burgdorferi* or *S. pyogenes*. It was proposed that the presence of a Pro residue within the Cys loop (position 304 in *B. anthracis*) in the K<sup>+</sup>-specific IMPDHs prevents the adaptation of the Cys loop to smaller monovalent cations.<sup>3</sup> Indeed, the Cys loop seems to be in the same orientation in all three *B. anthracis* structures presented here (Figure 4A,B). The three structures of the *B. anthracis* IMPDH represent the specific but static states of the enzyme, with no cofactor present and no reaction occurring. It is possible that because K<sup>+</sup> acts as the ball-and-socket joint facilitating the conformational changes, the presence of this ion is necessary during the reaction but not before (structure with IMP) or after (structure with XMP and P<sub>i</sub>) the reaction has occurred.

The active site of IMPDH can be subdivided into five subsites. Two of these subsites are occupied by IMP and XMP, with phosphosugar and purine base moieties. The NAD<sup>+</sup> binding site has the nicotinamide monophosphate binding subsite, the adenosine monophosphate binding subsite, and the pyrophosphate binding subsite. All *C. parvum* inhibitors are designed to occupy the NAD<sup>+</sup> site.<sup>39</sup> Kinetic characterization further localized binding to the nicotinamide monophosphate subsite.<sup>39</sup> Because *B. anthracis* IMPDH possesses the Ala253-Tyr445 minimal structural motif (*C. parvum* Ala165-Tyr358) that defines the susceptibility of the enzyme to *C. parvum* inhibitors, the protein is inhibited by inhibitors A110 and C91. Two other bacterial enzymes, those of *Ca. jejuni* and *Cl. perfringens*, also exhibit sensitivities to A110 and C91, whereas the *V. cholerae* protein, which does not contain the Ala165-Tyr358 motif, is not inhibited by these two compounds. The values of IC<sub>50</sub> and K<sub>D</sub> of A110 are within a factor of 2 for *B. anthracis*, *Ca. jejuni*, and *Cl. perfringens* enzymes, indicating that the binding sites of these compounds are conserved. Notably, the *Cl. perfringens* enzyme displays a different sensitivity to C91, with IC<sub>50</sub> and K<sub>D</sub> values approximately 10-fold higher than the corresponding values for the *B. anthracis* and *Ca. jejuni* enzymes. This suggests that C91 binds in a region that is conserved in *B. anthracis* and *Ca. jejuni* IMPDHs, but different in *Cl. perfringens*. It is important to mention that because the K<sub>D</sub> values obtained for the examined IMPDHs are proportional to the IC<sub>50</sub> values calculated in a conventional assay, BLI can be utilized as a convenient method for primary screening of inhibitor candidates.

Bacterial enzymes bind NAD<sup>+</sup> poorly (K<sub>m</sub> > 1 mM)<sup>3,74,75</sup> and are inhibited by MPA only at relatively high concentrations (K<sub>i</sub> > 3 μM). This suggests that the NAD<sup>+</sup> binding pocket is different in bacterial IMPDH. In *T. foetus* and human IMPDHs, the adenosine portion of NAD<sup>+</sup> is stacked with at least one aromatic and/or arginine residue (Arg241-Trp269 in *T. foetus*, Arg253-Tyr282 in human type I, and His253-Phe282 in human type II enzymes).<sup>16,21</sup> This stacking is not present in *B. anthracis* (Thr230-Gly259) or other bacteria. Other differences include the presence of a serine residue (*T. foetus* Ser263, human type I Ser275, and human type II Ser276) forming a hydrogen bond with the NAD<sup>+</sup> pyrophosphate group.<sup>21</sup> In *B. anthracis*, this residue is replaced with Ala253. All these differences may account for the lower affinity of the *B. anthracis* and other bacterial enzymes for NAD<sup>+</sup>. Interestingly, the overall

catalytic mechanism seems to remain the same. Bacterial IMPDH enzymes appear to favor a closed conformation (as shown in our phosphate ion-bound structure), in which the catalytic flap occupies the NAD<sup>+</sup> site. This closed conformation is needed for the hydrolysis step of the reaction. Therefore, it is possible that the bacterial enzymes, to increase the efficiency of hydrolysis, evolved toward a reduced affinity for the cofactor. This is consistent with the lower NAD<sup>+</sup> affinity and higher catalytic rate observed in bacterial IMPDH enzymes. Conversely, the mammalian IMPDH enzymes favor the open conformation. Accordingly, these display higher NAD<sup>+</sup> affinities and lower hydrolysis rates.

We have determined three crystal structures of *B. anthracis* IMPDH, a phosphate ion-bound (apo) form, one with substrate, IMP, and one with product, XMP. The P<sub>i</sub>-bound structure is the first bacterial structure with a complete active site flap. In this structure, the distal portion of the flap folds into the active site mimicking a closed conformation, which is required for the hydrolysis stage of the catalysis.

Rising microbial antibiotic resistance creates an urgent need for new drugs for the treatment of bacterial infections such as methicillin resistant *St. aureus* (MRSA). Because IMPDH is a crucial regulator of the intracellular guanine nucleotide pool, the inhibitors against IMPDH may strongly augment currently applied drugs against many other multidrug resistant strains even in cases where IMPDH is not essential. Some bacteria like *Ca. jejuni* lack the guanine salvage pathway, making their IMPDH enzymes an excellent targets for drug development. Thus, IMPDH inhibition offers a promising strategy for the development of broad-spectrum antibiotics.

Inhibition studies have, thus far, primarily focused on the active site, with inhibitors occupying the IMP or NAD<sup>+</sup> site. NAD<sup>+</sup>-based inhibitors that target the cofactor binding site can interact with three subsites, the nicotinamide monophosphate binding subsite, the adenosine monophosphate binding subsite, and the pyrophosphate binding subsite. The nicotinamide subsite of NAD<sup>+</sup> is highly conserved, and it is likely that more potent and selective inhibitors can be obtained by designing compounds that extend into the more diverged adenosine and pyrophosphate subsites. Because we observe that bacterial enzymes exhibit different sensitivities to the two tested *C. parvum* inhibitors, this study provides additional support for the strategy that prokaryotic IMPDH-specific inhibitors can be developed by focusing on the divergent portions of the NAD<sup>+</sup> site.

## ■ ASSOCIATED CONTENT

### ● Supporting Information

A size exclusion profile of the *B. anthracis* IMPDH (Figure S1). This material is available free of charge via the Internet at <http://pubs.acs.org>.

## ■ AUTHOR INFORMATION

### Corresponding Author

\*E-mail: andrzej@anl.gov. Phone: (630) 252-3926. Fax: (630) 252-6126.

### Funding

This work was supported by the National Institute of Allergy and Infectious Diseases, National Institutes of Health, Department of Health and Human Services, under Contract HHSN272200700058C, by National Institutes of Health Grants AI057153 (A.J.) and AI093459-01 (L.H.), and by the

U.S. Department of Energy, Office of Biological and Environmental Research, under Contract DE-AC02-06CH11357. This work has been created by UChicago Argonne, LLC, Operator of Argonne National Laboratory ("Argonne"). Argonne, a U.S. Department of Energy Office of Science laboratory, is operated under Contract DE-AC02-06CH11357. The U.S. Government retains for itself, and others acting on its behalf, a paid-up nonexclusive, irrevocable worldwide license in said article to reproduce, prepare derivative works, distribute copies to the public, and perform publicly and display publicly, by or on behalf of the Government.

## Notes

The authors declare no competing financial interest.

<sup>†</sup>Consultant, self-employed.

## ACKNOWLEDGMENTS

We thank all members of the Structural Biology Center at Argonne National Laboratory for their help in conducting these experiments, Lour Lezondra for help with the purification of IMPDH from *B. anthracis*, William Eschenfeldt for help with the preparation of an expression vector, and Lindy Keller for help in the preparation of the manuscript.

## ABBREVIATIONS

IMPDH, inosine 5'-monophosphate dehydrogenase; IMP, inosine 5'-monophosphate; NAD<sup>+</sup>, nicotinamide adenine dinucleotide; NADH, reduced nicotinamide adenine dinucleotide; XMP, xanthosine 5'-monophosphate; CBS, cystathionine  $\beta$ -synthase; P<sub>i</sub>, phosphate ion; MPA, mycophenolic acid; MZP, mizoribine 5'-monophosphate; RMP, ribavirin 5'-monophosphate; MAD, mycophenolic adenine nucleotide; rmsd, root-mean-square deviation; SAD, single-wavelength anomalous diffraction; TAD,  $\beta$ -methylene-thiazole-4-carboxamide adenine dinucleotide; BLI, biolayer interferometry; MRSA, methicillin resistant *St. aureus*.

## REFERENCES

- (1) Nair, V., and Shu, Q. (2007) Inosine Monophosphate Dehydrogenase as a Probe in Antiviral Drug Discovery. *Antiviral Chem. Chemother.* 18, 245.
- (2) Shu, Q., and Nair, V. (2008) Inosine monophosphate dehydrogenase (IMPDH) as a target in drug discovery. *Med. Res. Rev.* 28, 219–232.
- (3) Hedstrom, L. (2009) IMP Dehydrogenase: Structure, Mechanism, and Inhibition. *Chem. Rev.* 109, 2903–2928.
- (4) Weimert, N. A. P., DeRotte, M., Alloway, R. R. P., Woodle, E. S. M. D., and Vinks, A. A. P. P. (2007) Monitoring of Inosine Monophosphate Dehydrogenase Activity as a Biomarker for Mycophenolic Acid Effect: Potential Clinical Implications. *Ther. Drug Monit.* 29, 141–149.
- (5) Pankiewicz, K. W., Lesiak-Watanabe, K. B., Watanabe, K. A., Patterson, S. E., Jayaram, H. N., Yalowitz, J. A., Miller, M. D., Seidman, M., Majumdar, A., Prehna, G., and Goldstein, B. M. (2002) Novel Mycophenolic Adenine Bis(phosphonate) Analogues As Potential Differentiation Agents against Human Leukemia. *J. Med. Chem.* 45, 703–712.
- (6) Dhar, T. G. M., Shen, Z., Guo, J., Liu, C., Watterson, S. H., Gu, H. H., Pitts, W. J., Fleener, C. A., Rouleau, K. A., Sherbina, N. Z., McIntyre, K. W., Witmer, M. R., Tredup, J. A., Chen, B.-C., Zhao, R., Bednarz, M. S., Cheney, D. L., MacMaster, J. F., Miller, L. M., Berry, K. K., Harper, T. W., Barrish, J. C., Hollenbaugh, D. L., and Iwanowicz, E. J. (2002) Discovery of N-[2-[2-[[3-Methoxy-4-(5-oxazolyl)phenyl]-amino]-5-oxazolyl]phenyl]-N-methyl-4-morpholineacetamide as a Novel and Potent Inhibitor of Inosine Monophosphate Dehydrogenase with Excellent in Vivo Activity. *J. Med. Chem.* 45, 2127–2130.

- (7) Hedstrom, L., Liechti, G., Goldberg, J. B., and Gollapalli, D. R. (2011) The Antibiotic Potential of Prokaryotic IMP Dehydrogenase Inhibitors. *Curr. Med. Chem.* 18, 1909–1918.
- (8) Maher, C., and Lushniak, B. D. (2009) Availability of Medical Countermeasures for Bioterrorism Events: US Legal and Regulatory Options. *Clin. Pharmacol. Ther.* 85, 669–671.
- (9) Franco, C., and Sell, T. K. (2011) Federal Agency Biodefense Funding, FY2011-FY2012. *Biosecurity and Bioterrorism: Biodefense Strategy, Practice, and Science* 9, 117–137.
- (10) Bentley, R. (2000) Mycophenolic Acid: A One Hundred Year Odyssey from Antibiotic to Immunosuppressant. *Chem. Rev.* 100, 3801–3826.
- (11) Abraham, E. P. (1945) The effect of mycophenolic acid on the growth of *Staphylococcus aureus* in heart broth. *Biochem. J.* 39, 398–408.
- (12) Florey, H. W., Jennings, M. A., Gilliver, K., and Sanders, A. G. (1946) Mycophenolic Acid, an Antibiotic from *Penicillium brevicompactum* Dierckx. *Lancet* 247, 46–49.
- (13) Sintchak, M. D., Fleming, M. A., Futer, O., Raybuck, S. A., Chambers, S. P., Caron, P. R., Murcko, M. A., and Wilson, K. P. (1996) Structure and mechanism of inosine monophosphate dehydrogenase in complex with the immunosuppressant mycophenolic acid. *Cell* 85, 921–930.
- (14) Whitby, F. G., Luecke, H., Kuhn, P., Somoza, J. R., Huete-Perez, J. A., Phillips, J. D., Hill, C. P., Fletterick, R. J., and Wang, C. C. (1997) Crystal structure of *Tritrichomonas foetus* inosine-5'-monophosphate dehydrogenase and the enzyme-product complex. *Biochemistry* 36, 10666–10674.
- (15) Zhang, R., Evans, G., Rotella, F. J., Westbrook, E. M., Beno, D., Huberman, E., Joachimiak, A., and Collart, F. R. (1999) Characteristics and crystal structure of bacterial inosine-5'-monophosphate dehydrogenase. *Biochemistry* 38, 4691–4700.
- (16) Colby, T. D., Vanderveen, K., Strickler, M. D., Markham, G. D., and Goldstein, B. M. (1999) Crystal structure of human type II inosine monophosphate dehydrogenase: Implications for ligand binding and drug design. *Proc. Natl. Acad. Sci. U.S.A.* 96, 3531–3536.
- (17) McMillan, F. M., Cahoon, M., White, A., Hedstrom, L., Petsko, G. A., and Ringe, D. (2000) Crystal structure at 2.4 Å resolution of *Borrelia burgdorferi* inosine 5'-monophosphate dehydrogenase: Evidence of a substrate-induced hinged-lid motion by loop 6. *Biochemistry* 39, 4533–4542.
- (18) Prosis, G. L., Wu, J. Z., and Luecke, H. (2002) Crystal structure of *Tritrichomonas foetus* inosine monophosphate dehydrogenase in complex with the inhibitor ribavirin monophosphate reveals a catalysis-dependent ion-binding site. *J. Biol. Chem.* 277, 50654–50659.
- (19) Gan, L., Petsko, G. A., and Hedstrom, L. (2002) Crystal structure of a ternary complex of *Tritrichomonas foetus* inosine 5'-monophosphate dehydrogenase: NAD<sup>+</sup> orients the active site loop for catalysis. *Biochemistry* 41, 13309–13317.
- (20) Gan, L., Seyedsayamdost, M. R., Shuto, S., Matsuda, A., Petsko, G. A., and Hedstrom, L. (2003) The immunosuppressive agent mizoribine monophosphate forms a transition state analogue complex with inosine monophosphate dehydrogenase. *Biochemistry* 42, 857–863.
- (21) Prosis, G. L., and Luecke, H. (2003) Crystal structures of *Tritrichomonas foetus* inosine monophosphate dehydrogenase in complex with substrate, cofactor and analogs: A structural basis for the random-in ordered-out kinetic mechanism. *J. Mol. Biol.* 326, 517–527.
- (22) MacPherson, I. S., Kirubakaran, S., Gorla, S. K., Riera, T. V., D'Aquino, J. A., Zhang, M., Cuny, G. D., and Hedstrom, L. (2010) The Structural Basis of *Cryptosporidium*-Specific IMP Dehydrogenase Inhibitor Selectivity. *J. Am. Chem. Soc.* 132, 1230–1231.
- (23) Wierenga, R. K. (2001) The TIM-barrel fold: A versatile framework for efficient enzymes. *FEBS Lett.* 492, 193–198.
- (24) Bateman, A. (1997) The structure of a domain common to archaeobacteria and the homocystinuria disease protein. *Trends Biochem. Sci.* 22, 12–13.



- (25) Ignoul, S., and Eggermont, J. (2005) CBS domains: Structure, function, and pathology in human proteins. *Am. J. Physiol.* 289, C1369–C1378.
- (26) Hedstrom, L., and Gan, L. (2006) IMP dehydrogenase: Structural schizophrenia and an unusual base. *Curr. Opin. Chem. Biol.* 10, 520–525.
- (27) Pankiewicz, K. W., and Goldstein, B. M. (2003) Inosine Monophosphate Dehydrogenase and Its Inhibitors: An Overview. In *Inosine Monophosphate Dehydrogenase: A Major Therapeutic Target*, pp 1–17, American Chemical Society, Washington, DC.
- (28) Guillen Schlippe, Y. V., and Hedstrom, L. (2005) A twisted base? The role of arginine in enzyme-catalyzed proton abstractions. *Arch. Biochem. Biophys.* 433, 266–278.
- (29) Min, D., Josephine, H. R., Li, H., Lakner, C., MacPherson, I. S., Naylor, G. J. P., Swofford, D., Hedstrom, L., and Yang, W. (2008) An Enzymatic Atavist Revealed in Dual Pathways for Water Activation. *PLoS Biol.* 6, 1802–1810.
- (30) Xiang, B., Taylor, J. C., and Markham, G. D. (1996) Monovalent Cation Activation and Kinetic Mechanism of Inosine 5'-Monophosphate Dehydrogenase. *J. Biol. Chem.* 271, 1435–1440.
- (31) Markham, G. D. (2003) Monovalent Cation Activation of IMP Dehydrogenase. *ACS Symp. Ser.* 839, 169–183.
- (32) Zhang, R., Evans, G., Rotella, F., Westbrook, E., Huberman, E., Joachimiak, A., and Collart, F. R. (1999) Differential signatures of bacterial and mammalian IMP dehydrogenase enzymes. *Curr. Med. Chem.* 6, 537–543.
- (33) Fleming, M. A., Chambers, S. P., Connelly, P. R., Nimmesgern, E., Fox, T., Bruzzese, F. J., Hoe, S. T., Fulghum, J. R., Livingston, D. J., Stuver, C. M., Sintchak, M. D., Wilson, K. P., and Thomson, J. A. (1996) Inhibition of IMPDH by Mycophenolic Acid: A Dissection of Forward and Reverse Pathways Using Capillary Electrophoresis. *Biochemistry* 35, 6990–6997.
- (34) Link, J. O., and Straub, K. (1996) Trapping of an IMP Dehydrogenase-Substrate Covalent Intermediate by Mycophenolic Acid. *J. Am. Chem. Soc.* 118, 2091–2092.
- (35) Digits, J. A., and Hedstrom, L. (2000) Drug Selectivity Is Determined by Coupling Across the NAD<sup>+</sup> Site of IMP Dehydrogenase. *Biochemistry* 39, 1771–1777.
- (36) Striepen, B., Puijssers, A. J. P., Huang, J., Li, C., Gubbels, M.-J., Umejiego, N. N., Hedstrom, L., and Kissinger, J. C. (2004) Gene transfer in the evolution of parasite nucleotide biosynthesis. *Proc. Natl. Acad. Sci. U.S.A.* 101, 3154–3159.
- (37) Striepen, B., White, M. W., Li, C., Guerini, M. N., Malik, S.-B., Logsdon, J. M., Liu, C., and Abrahamsen, M. S. (2002) Genetic complementation in apicomplexan parasites. *Proc. Natl. Acad. Sci. U.S.A.* 99, 6304–6309.
- (38) Gollapalli, D. R., MacPherson, I. S., Liechti, G., Gorla, S. K., Goldberg, J. B., and Hedstrom, L. (2010) Structural Determinants of Inhibitor Selectivity in Prokaryotic IMP Dehydrogenases. *Chem. Biol.* 17, 1084–1091.
- (39) Umejiego, N. N., Gollapalli, D., Sharling, L., Volftsun, A., Lu, J., Benjamin, N. N., Stroupe, A. H., Riera, T. V., Striepen, B., and Hedstrom, L. (2008) Targeting a Prokaryotic Protein in a Eukaryotic Pathogen: Identification of Lead Compounds against Cryptosporidiosis. *Chem. Biol.* 15, 70–77.
- (40) Maurya, S. K., Gollapalli, D. R., Kirubakaran, S., Zhang, M., Johnson, C. R., Benjamin, N. N., Hedstrom, L., and Cuny, G. D. (2009) Triazole Inhibitors of *Cryptosporidium parvum* Inosine 5'-Monophosphate Dehydrogenase. *J. Med. Chem.* 52, 4623–4630.
- (41) Sharling, L., Liu, X., Gollapalli, D. R., Maurya, S. K., Hedstrom, L., and Striepen, B. (2010) A Screening Pipeline for Antiparasitic Agents Targeting *Cryptosporidium* Inosine Monophosphate Dehydrogenase. *PLoS Neglected Trop. Dis.* 4, 1–12.
- (42) Stols, L., Gu, M., Dieckman, L., Raffin, R., Collart, F. R., and Donnelly, M. I. (2002) A new vector for high-throughput, ligation-independent cloning encoding a tobacco etch virus protease cleavage site. *Protein Expression Purif.* 25, 8–15.
- (43) Walsh, M. A., Dementieva, I., Evans, G., Sanishvili, R., and Joachimiak, A. (1999) Taking MAD to the extreme: Ultrafast protein structure determination. *Acta Crystallogr. D55*, 1168–1173.
- (44) Eschenfeldt, W., Maltseva, N., Stols, L., Donnelly, M., Gu, M., Nocek, B., Tan, K., Kim, Y., and Joachimiak, A. (2010) Cleavable C-terminal His-tag vectors for structure determination. *J. Struct. Funct. Genomics* 11, 31–39.
- (45) Beckett, D., Kovaleva, E., and Schatz, P. J. (1999) A minimal peptide substrate in biotin holoenzyme synthetase-catalyzed biotinylation. *Protein Sci.* 8, 921–929.
- (46) Kim, Y., Babnigg, G., Jedrzejczak, R., Eschenfeldt, W. H., Li, H., Maltseva, N., Hatzos-Skintges, C., Gu, M., Makowska-Grzyska, M., Wu, R., An, H., Chhor, G., and Joachimiak, A. (2011) High-throughput protein purification and quality assessment for crystallization. *Methods* 55, 12–28.
- (47) Rosenbaum, G., Alkire, R. W., Evans, G., Rotella, F. J., Lazarski, K., Zhang, R. G., Ginell, S. L., Duke, N., Naday, I., Lazarski, J., Molitsky, M. J., Keefe, L., Gonczy, J., Rock, L., Sanishvili, R., Walsh, M. A., Westbrook, E., and Joachimiak, A. (2006) The Structural Biology Center 191D undulator beamline: Facility specifications and protein crystallographic results. *J. Synchrotron Radiat.* 13, 30–45.
- (48) Minor, W., Cymborowski, M., Otwinowski, Z., and Chruszcz, M. (2006) HKL-3000: The integration of data reduction and structure solution—from diffraction images to an initial model in minutes. *Acta Crystallogr. D62*, 859–866.
- (49) Schneider, T. R., and Sheldrick, G. M. (2002) Substructure solution with SHELXD. *Acta Crystallogr. D58*, 1772–1779.
- (50) Winn, M. D., Isupov, M. N., and Murshudov, G. N. (2001) Use of TLS parameters to model anisotropic displacements in macromolecular refinement. *Acta Crystallogr. D57*, 122–133.
- (51) Cowtan, K. (1994) *Joint CCP4 and ESF-EACBM Newsletter on Protein Crystallography*, 34–38.
- (52) Morris, R. J., Perrakis, A., and Lamzin, V. S. (2003) ARP/wARP and automatic interpretation of protein electron density maps. *Methods Enzymol.* 374, 229–244.
- (53) Emsley, P., and Cowtan, K. (2004) Coot: Model-building tools for molecular graphics. *Acta Crystallogr. D60*, 2126–2132.
- (54) Collaborative Computational Project, Number 4 (1994) The CCP4 suite: Programs for protein crystallography. *Acta Crystallogr. D50*, 760–763.
- (55) Adams, P. D., Afonine, R. V., Bunkoczi, G., Chen, V. B., Echols, N., Headd, J. J., Hung, L.-W., Kapral, G. J., Grosse-Kunstleve, R. W., McCoy, A. J., Moriarty, N. W., Oeffner, R., Read, R. J., Richardson, D. C., Richardson, J. S., Terwilliger, T. C., and Zwart, P. H. (2010) PHENIX: A comprehensive Python-based system for macromolecular structure solution. *Acta Crystallogr. D66*, 213–221.
- (56) Murshudov, G. N., Vagin, A. A., and Dodson, E. J. (1997) Refinement of Macromolecular Structures by the Maximum-Likelihood Method. *Acta Crystallogr. D53*, 240–255.
- (57) Laskowski, R. A., MacArthur, M. W., Moss, D. S., and Thornton, J. M. (1993) PROCHECK: A program to check the stereochemical quality of protein structures. *J. Appl. Crystallogr.* 26, 283–291.
- (58) Davis, I. W., Leaver-Fay, A., Chen, V. B., Block, J. N., Kapral, G. J., Wang, X., Murray, L. W., Arendall, W. B., III, Snoeyink, J., Richardson, J. S., and Richardson, D. C. (2007) MolProbity: All-atom contacts and structure validation for proteins and nucleic acids. *Nucleic Acids Res.* 35, W375–W383.
- (59) Kerr, K. M., Digits, J. A., Kuperwasser, N., and Hedstrom, L. (2000) Asp338 controls hydride transfer in *Escherichia coli* IMP dehydrogenase. *Biochemistry* 39, 9804–9810.
- (60) Schmitt, H.-M., Brecht, A., Piehler, J., and Gauglitz, G. (1997) An integrated system for optical biomolecular interaction analysis. *Biosens. Bioelectron.* 12, 809–816.
- (61) Krissinel, E., and Henrick, K. (2004) Secondary-structure matching (SSM), a new tool for fast protein structure alignment in three dimensions. *Acta Crystallogr. D60*, 2256–2268.
- (62) Kerr, K. M., Cahoon, M., Bosco, D. A., and Hedstrom, L. (2000) Monovalent Cation Activation in *Escherichia coli* Inosine 5'-Monophosphate Dehydrogenase. *Arch. Biochem. Biophys.* 375, 131–137.

- (63) Zhou, X., Cahoon, M., Rosa, P., and Hedstrom, L. (1997) Expression, Purification, and Characterization of Inosine 5'-Monophosphate Dehydrogenase from *Borrelia burgdorferi*. *J. Biol. Chem.* 272, 21977–21981.
- (64) Umejiego, N. N., Li, C., Riera, T., Hedstrom, L., and Striepen, B. (2004) *Cryptosporidium parvum* IMP Dehydrogenase: Identification of functional, structural, and dynamic properties that can be exploited for drug design. *J. Biol. Chem.* 279, 40320–40327.
- (65) Digits, J. A., and Hedstrom, L. (1999) Species-Specific Inhibition of Inosine 5'-Monophosphate Dehydrogenase by Mycophenolic Acid. *Biochemistry* 38, 15388–15397.
- (66) Cheng, Y.-C., and Prusoff, W. H. (1973) Relationship between the inhibition constant ( $K_i$ ) and the concentration of inhibitor which causes 50% inhibition ( $I_{50}$ ) of an enzymatic reaction. *Biochem. Pharmacol.* 22, 3099–3108.
- (67) Burlingham, B. T., and Widlanski, T. S. (2003) An Intuitive Look at the Relationship of  $K_i$  and  $IC_{50}$ : A More General Use for the Dixon Plot. *J. Chem. Educ.* 80, 214.
- (68) Cooper, M. A. (2006) Optical biosensors: Where next and how soon? *Drug Discovery Today* 11, 1061–1067.
- (69) Small Molecule Binding Kinetics. Technical Note 16, ForteBio Home Page.
- (70) Xiang, B., and Markham, G. D. (1997) Probing the mechanism of inosine monophosphate dehydrogenase with kinetic isotope effects and NMR determination of the hydride transfer stereospecificity. *Arch. Biochem. Biophys.* 348, 378–382.
- (71) Hedstrom, L. (1999) IMP dehydrogenase: Mechanism of action and inhibition. *Curr. Med. Chem.* 6, 545–560.
- (72) Antonino, L. C., and Wu, J. C. (1994) Human IMP dehydrogenase catalyzes the dehalogenation of 2-fluoro- and 2-chloro-inosine 5'-monophosphate in the absence of NAD. *Biochemistry* 33, 1753–1759.
- (73) Riera, T. V., Zheng, L., Josephine, H. R., Min, D., Yang, W., and Hedstrom, L. (2011) Allosteric Activation via Kinetic Control: Potassium Accelerates a Conformational Change in IMP Dehydrogenase. *Biochemistry* 50, 8508–8518.
- (74) Braun-Perez, S. B., and Peetz, M. (2010) Inosine monophosphate dehydrogenase as a target for antiviral, anticancer, antimicrobial, and immunosuppressive therapeutics. *Future Med. Chem.* 2, 81–92.
- (75) Pimkin, M., and Markham, G. D. (2009) Inosine 5'-monophosphate dehydrogenase. *Adv. Enzymol. Relat. Areas Mol. Biol.* 76, 1–53.